Technical Memo

ECMWF
European Centre for Medium-Range Weather Forecasts

903

Validation of IFS+RTTOV/MFASIS 0.64-μm reflectances against observations from GOES-16, GOES-17, MSG-4 and Himawari-8

Philippe Lopez and Marco Matricardi

September 2022

Series: ECMWF Technical Memoranda

A full list of ECMWF Publications can be found on our website under:
http://www.ecmwf.int/en/publications

Contact: library@ecmwf.int

European Centre for Medium-Range Weather Forecasts, Shinfield Park, Reading, RG2 9AX, UK

Abstract

Reflectances simulated by running RTTOV/MFASIS on input meteorological fields from ECMWF's operational IFS short-range forecasts are compared to observations in the 0.64-μm channel of the MSG-4, Himawari-8, GOES-16, and GOES-17 geostationary satellite imagers. This work is an extension to multiple geostationary satellites of the validation focused on GOES-16, which was recently described in Lopez *et al.* (2022). A comparison of validation results obtained with input data from operational forecasts from IFS versions 47R3 and 47R1 is also presented.

Month-long statistics of reflectances are used to identify deficiencies in both the IFS and in the RTTOV/MFASIS radiative transfer model. This study confirms the existence of biases resulting from simplifications in RTTOV/MFASIS, such as those made in the Rayleigh scattering computations, and from the use of a look-up table. These biases mainly affect regions with low solar elevation. As for the IFS, the two main issues relate to the representation of trade-wind low-level clouds over tropical oceans, with an underprediction of marine stratocumuli on their eastern side, and oversized cloud clusters in their central part. Other systematic discrepancies between the IFS and observations are evidenced over Africa, during both the dry season (excessive shallow convection over Ethiopian Highlands) and the rainy season (occasional poor representation of squall lines over the Sahel; excessive cloud amounts from Guinea to the Ivory Coast). In other respects, prescribing land surface reflectance properties from a monthly atlas is found to yield a reasonable agreement between simulated and observed clear-sky reflectances during the investigated period.

This work can be seen as a preliminary step towards the assimilation of visible reflectances in ECMWF's 4-Dimensional Variational data assimilation (4D-Var) system.

Plain Language Summary

It has recently become possible to simulate images of Earth as they would be collected by a satellite observing the visible light reflected by our planet's surface and atmosphere (including clouds). One way to achieve this is by running the RTTOV/MFASIS software on meteorological data coming from the ECMWF's numerical weather forecasting system (the IFS). The comparison of simulated and satellite images allows the identification of inaccuracies not only in RTTOV/MFASIS, but also in the weather forecast model.

In this study, such an evaluation is performed against four weather-observing satellites, over one winter and one summer month in 2021. Despite the overall fairly good agreement between simulated and observed images, some simplifications made in RTTOV/MFASIS are found to lead to some noticeable discrepancies, especially near sunrise and sunset. On the other hand, the largest inaccuracies in the numerical weather prediction model relate to low-level clouds over tropical oceans, as well as tropical storms over land, especially over West Africa. A comparison of the two most recent versions of the IFS (47R1 and 47R3) is also presented.

By documenting our ability to simulate the visible light reflected by our planet as viewed from space, this work also paves the way to the future blending of model data with satellite visible-light observations for improving our description of the 3D atmospheric state at past or present times (through the so-called "data assimilation" procedure).

1 Introduction

Among the wide range of frequencies used by satellite instruments to observe Earth's atmosphere, shortwave (solar spectrum) frequencies have been largely underused in Numerical Weather Prediction (NWP) applications so far, compared with longwave (infrared) and microwave wavelengths. Observations at visible wavelengths can provide valuable additional information about clouds (esp. low-level clouds)

and aerosols, that is not available from infrared or microwave data.

One of the solar-spectrum reflectance simulators that recently became available is the Method for FAst Satellite Image Synthesis (MFASIS; Scheck *et al.*, 2016), which uses an 8-dimensional look-up table. The recent integration of MFASIS in RTTOV (Radiative Transfer for TOVS; Saunders *et al.*, 2018) has made it possible to simulate solar reflectances in individual channels of specific satellites. Using this approach, Steele *et al.* (2022) performed a preliminary monitoring of simulated reflectances from IFS short-range forecasts against OLCI (Ocean and Land Colour Imager) observations from two polar-orbiting Sentinel satellites. Geostationary satellites are also of particular interest because their wide field of view (FOV) can encompass extremely varied meteorological situations in a single image. Lopez *et al.* (2022) (LMF22, hereafter) recently presented a first validation of solar-spectrum reflectances simulated by running RTTOV/MFASIS on input operational IFS forecast data, against observations from GOES-16 ABI.

The present study extends the latter validation to three other geostationary instruments: MSG-4 SEVIRI, Himawari-8 AHI and GOES-17 ABI, over similar two 1-month-long periods focusing on the 0.64-μm channel (because of its smaller biases in RTTOV/MFASIS, as shown in LMF22). Considering four satellites has the advantage of providing a validation covering most of the globe, besides polar regions. The main purpose is to identify possible deficiencies in both the IFS forecast model and the RTTOV/MFASIS reflectance simulator. In addition to its potential usefulness for improving the forecast model itself (physical parametrizations), this study can also provide guidance in the work towards the assimilation of visible reflectances at ECMWF, especially with regard to the expected performance of the observation operator and the requirements for data screening.

First, section 2 introduces the observations, the IFS model data and the RTTOV/MFASIS solar reflectance simulator used in this study. After a brief description of the mean circulation and cloud cover during the selected two periods, section 3 provides a statistical analysis of the validation of simulated versus observed reflectances, when using operational forecast data from IFS version 47R1. Validation results for IFS versions 47R3 and 47R1 against each satellite are then intercompared, to document the impact of the in-depth revision of the moist physics implemented in IFS version 47R3 (used in ECMWF's operations since 12 October 2021). Finally, section 4 analyzes the dominant systematic errors by focusing on individual dates and specific regions of the globe. A tentative assessment of the relevance of the land surface reflectance properties prescribed in the monthly atlas used in RTTOV is also presented. Summary and conclusions are given in section 5.

2 Data and methodology

2.1 Geostationary satellite observations

The 0.64-μm reflectance observations used in this study come from the imagers on board four geostationary satellites: MSG-4 (alias Meteosat-11; EUMETSAT[1]), Himawari-8 (JMA[2]), GOES-16 (NOAA[3]) and GOES-17 (NOAA). The respective imagers on board MSG, Himawari, and GOES are SEVIRI (Spinning Enhanced Visible Infra-Red Imager), AHI (Advanced Himawari Imager) and ABI (Advanced Baseline Imager). The main characteristics of these instruments and observations are summarized in Table 1 and more details can be found in Schmid (2000); JMA (2017); Schmit *et al.* (2005, 2017). The field of

[1]European Organization for the Exploitation of Meteorological Satellites
[2]Japan Meteorological Agency
[3]National Oceanic and Atmospheric Administration (USA)

view of each imager is displayed in Fig.1. MSG SEVIRI Level-1.5 native format reflectance data were

Satellite	Instrument	Central wavelength [μm]	Sub-satellite resolution [km]	Sub-satellite longitude [deg]
MSG-4	SEVIRI	0.635	3.0	0.0
Himawari-8	AHI	0.645	0.5	140.7
GOES-16	ABI	0.640	0.5	-75.2
GOES-17	ABI	0.640	0.5	-137.2

Table 1: Main information about the four geostationary satellites used in this study.

retrieved from EUMETSAT Data Store (https://data.eumetsat.int/), while GOES ABI netCDF Level-1b radiance data were accessed via NOAA's CLASS[4]. Himawari AHI reflectances were obtained from JMA via Jérôme Vidot of CEMS[5]. Note that infrared window channel data have also occasionally been used in the present work to provide ancillary information about cloud top heights, when investigating individual cases. In addition, GOES ABI netCDF Level-2 products (cloud mask and aerosol optical depths from CLASS) have been employed to identify clear-sky situations.

Prior to statistical computations, observed 0.64-μm reflectances have been spatially averaged to match the output grid of the IFS+RTTOV/MFASIS simulator (IRM, hereafter; see section 2.3).

2.2 IFS model data

The validation proposed in this study focuses on short-range forecasts obtained with ECMWF's operational IFS (Integrated Forecasting System; Courtier *et al.*, 1994) at a resolution of 9 km and initialized at 0000 UTC. To cover various weather regimes, the validation is performed over two periods: 15 January-15 February 2021 and 15 July-15 August 2021. For both periods, the forecast data are based on version 47R1 of the IFS (documentation available from *https://www.ecmwf.int/en/publications*), which was operational between 30 June 2020 and 12 October 2021. Similar forecast data from the pre-operational parallel suite based on version 47R3 of the IFS are also used to identify improvements and degradations with respect to version 47R1, especially those resulting from the major revision of the moist physics package in 47R3 (Bechtold *et al.*, 2020). For each satellite, the present report focuses on forecast valid times that are the nearest to local noon at the sub-satellite point (SSP), namely 1200 UTC for MSG-4, 1700 UTC for GOES-16, 2100 UTC for GOES-17 and 0300 UTC for Himawari-8. This is to maximize the coverage in visible data. It should also be noted that short forecast ranges are selected here in order to match the typical length of forecasts that provide the background information used in 4D-Var data assimilation.

2.3 RTTOV/MFASIS reflectance simulator

The simulation of reflectances from IFS forecast data relies on the lookup-table-based radiative transfer model MFASIS (Method for FAst Satellite Image Synthesis) developed by Scheck *et al.* (2016). The recent implementation of MFASIS in RTTOV (Radiative Transfer for TOVS; Saunders *et al.*, 2018) allows the simulation of reflectances in selected channels from IFS input data, in the way they would be measured by a given space-borne instrument. In particular, the instrument's actual response function for

[4]Comprehensive Large Array-data Stewardship System
[5]Centre d'Etudes en Météorologie Satellitaire, France

each channel can be taken into account in the radiative transfer computations. Results from this study have been obtained using RTTOV version 12.2.

2.3.1 Inputs

The required input IFS data are three-dimensional model-level fields of temperature, specific humidity, cloud fraction, cloud liquid water, cloud ice and snow content; plus the following two-dimensional fields (mostly surface): land-sea mask, logarithm of surface pressure, sea ice cover, snow depth, snow density, skin temperature, 10-metre meridional and zonal wind components, 2-metre dry-bulb and dew-point temperatures, and convective available potential energy (CAPE).

2.3.2 Special features

Compared with the original version of RTTOV/MFASIS used at ECMWF, a few additional features had to be added to make computations more realistic, namely

- a simple parametrization of reflectances over snow-covered land, including the effect of high vegetation;
- the activation of RTTOV's sunglint parametrization over sea, using the wave spectrum model of Elfouhaily *et al.* (1997);
- the use of the atlas of mean monthly land BRDF (Bidirectional Reflectance Distribution Function) of Vidot and Borbás (2014).

More details on these refinements can be found in LMF22.

2.3.3 Assumptions and limitations

In the current version of RTTOV/MFASIS used at ECMWF, cloud ice and snow are assumed to have the same optical properties and their respective contents are simply added before calculating the effective diameter of ice particles used in the radiative calculations. Furthermore, ice particle effective radii are specified following McFarquhar *et al.* (2003) and resulting ice optical properties are parametrized according to Baum *et al.* (2011). For liquid water clouds, the Optical Properties of Aerosols and Clouds (OPAC) package of Hess *et al.* (1998) is selected. In the OPAC framework, four warm cloud types (convective or stratiform; over land or sea) are distinguished to specify effective particle radii and derive optical properties from cloud liquid water contents, assuming a modified gamma distribution for particle size. Furthermore, it is important to stress that ECMWF's current version of RTTOV/MFASIS ignores the influence of both molecular absorption and aerosols on reflectances. At the 0.64-μm wavelength, molecular absorption should be negligible, while the overall influence of aerosols is expected to remain small (less than 2% in reflectance units), outside dry-season biomass burning events in Africa and in the Amazon region, and sandstorms.

The version of MFASIS implemented in RTTOV v12.2 involves an eight-dimensional look-up table (LUT). The eight parameters of the LUT are: solar zenith angle θ_{sun}, satellite zenith angle θ_{sat}, scattering angle (i.e., the angle between incident and scattered directions), surface albedo, cloud liquid and ice optical depths and associated effective radii. As emphasized in Scheck *et al.* (2016), the use of an LUT does imply interpolation errors, which, however, remain small as long as θ_{sun} and θ_{sat} do not exceed 85° (i.e., just after sunrise or just before sunset, or close to the edge of the geostationary satellite's FOV).

Errors in such special conditions can be made worse by the fact that MFASIS operates on individual vertical profiles and thus neglects 3D radiative effects, such as those associated with cloud overlap, shadows and sloping cloud tops. Situations with zenith angles above 85° are therefore discarded from the statistical validation of IRM presented here.

A further limitation comes from the fact that in the version of MFASIS used here, Rayleigh scattering computations (1) only account for single scattering and (2) assume a fixed cloud top height for liquid water and ice cloud layers (4 and 8 km, respectively).

2.3.4 Outputs

The simulator outputs reflectances on a grid whose spacing varies linearly with satellite viewing angle. The resolution of this output grid is specified to match the resolution of operational deterministic forecasts (9 km) at SSP. The actual resolution (in km) of the output grid becomes coarser when satellite viewing angle increases (i.e., towards the limb).

3 Validation results

Before presenting statistical results of the validation, it is assumed that (1) errors in observed reflectances (e.g., instrumental errors, geolocation errors) are small and (2) mismatches between IRM and observed reflectances originate from errors either in the RTTOV/MFASIS radiative transfer itself or in its input meteorological fields forecast by the IFS.

3.1 Background meteorology

To summarize the general circulation for each period of interest, Fig.1 displays maps of mean-sea-level pressure (MSLP) and total cloud cover, obtained from ECMWF's operational archive. Averages are based on six-hourly analyses for MSLP, and on hourly outputs from 24h-range forecast started at 0000 UTC for total cloud cover. The boundary of the field of view of each geostationary satellite is also shown. As expected, high pressures dominate over subtropical oceans in both periods, and over North America and Northern Asia in the winter (Fig.1a). The Southern Hemisphere (SH) anticyclones are stronger during the local winter (Fig.1c). The usual wintertime strong dipole in MSLP over the North Atlantic and North Pacific can easily be identified in Fig.1a. Low pressures dominate over southern polar regions as well as in the intertropical band, in both periods. In the latter region, the minimum of MSLP over the oceans is centered about the equator during the NH winter (Fig.1a), but moves north of the equator during the NH summer, reaching the Tropic of Cancer over Africa and Asia (Fig.1c). Note that the seemingly higher pressure values over steep mountains (e.g., Andes, Himalayas) are likely to be an artefact of uncertainties associated with below-ground extrapolation in the conversion of surface pressure to MSLP.

As far as mean total cloud cover is concerned, Fig.1b,d offers a reminder of the predominance of clouds ($>$0.7) (1) over extratropical regions in both periods, (2) over the Amazon basin, Central Africa, India and South-East Asia during the rainy season, as well as (3) on the eastern side of subtropical marine anticyclones (especially over the Pacific Ocean). Substantial cloud cover (between 0.6 and 0.9) is also associated with the narrow intertropical convergence zone (ITCZ) over oceans. In contrast, low values of cloud cover ($<$0.4) dominate in both seasons (Fig.1b,d) over most deserts (Sahara, Namibia, Arabia,

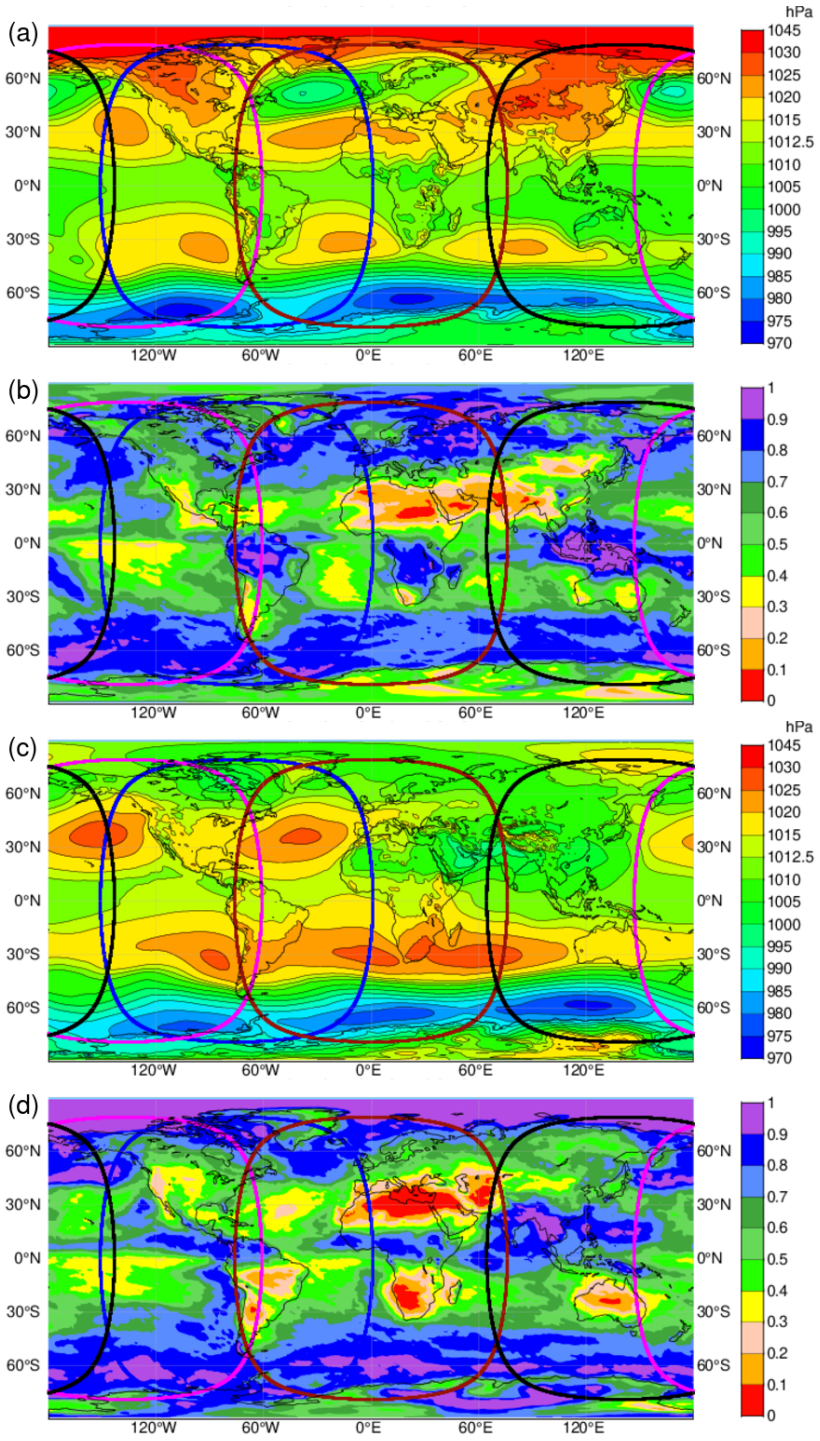

Figure 1: (a,c) Mean-sea-level pressure (MSLP; in hPa) and (b,d) mean total cloud cover (unitless) over each of the two selected periods (a,b) 15 January-15 February 2021 and (b,d) 15 July-15 August 2021. Averaging was performed on ECMWF's operational daily six-hourly analyses for MSLP, and daily hourly forecasts started at 0000 UTC for total cloud cover. The boundary of the field of view of each geostationary satellite is also shown: MSG-4 (brown); Himawari-8 (black); GOES-16 (dark blue); GOES-17 (purple).

Atacama), and to a lesser extent over the South-East United States and western Mexico, as well as on the western flank of tropical oceans. Mean total cloud cover is also below 0.3 over the Australian Desert in the SH winter (Fig.1d), as well as over India in the NH winter (Fig.1b).

3.2 Statistical analysis for IFS version 47R1

3.2.1 Mean biases

Figure 2 displays maps of mean IRM−observation 0.64-μm reflectance biases (expressed in units of reflectance) for the two selected periods (columns) and for the four satellites considered (rows). Again, it is reminded that the validation time for each satellite corresponds to SSP local noon, to maximize the sunlit fraction of the field of view.

Figure 2 confirms the existence of a systematic negative bias in IRM near the terminator (i.e. the twilight zone) against all satellites. This bias was indeed already highlighted in LMF22 and was attributed to increased interpolation errors in MFASIS LUT for very low sun elevations. In contrast, away from the terminator, most tropical oceans are affected by an overestimation of about 5% (blue shading) of reflectances in IRM. LMF22 attributed this bias to the prediction of low-level cumulus clouds whose horizontal size is far too large, and whose closed-cell organization disagrees with the open-cell convection found on satellite images. In Fig.2e,f, IRM's marked overestimation of reflectances by several tens of % (in reflectance units) (red shading) on the eastern flank of the South Pacific High was shown by LMF22 to be associated with a systematic under-prediction of trade-wind low-level clouds in the IFS. This negative bias is particularly strong during the SH winter off the Peruvian and Chilean coasts (reaching -50% in reflectance units). A similar, although weaker (around -5%), negative reflectance bias in IRM can also be identified over the Atlantic Ocean, off the Moroccan and Angolan coasts during the NH summer (Fig.2b).

Over land, the most noticeable signals are an overestimation of reflectances (by up to 10%) by IRM over west African countries during the local rainy season, from Gabon to Namibia in the NH winter (Fig.2a), and from Senegal to Liberia in the NH summer (Fig.2b). Another sizeable bias affects the Ethiopian Highlands, with an overestimation of reflectances during the NH winter in Fig.2a. In the NH summer, the same region exhibits a tripolar pattern: positive biases over inland Somalia and the Ogaden plain are surrounded by two regions with negative biases, the first one over the Ethiopian Highlands, the second on the Somali coast (Fig.2b). A further insight into the biases over this particular region of Africa will be given in section 4. The Amazon Basin exhibits an underestimation in the west (up to the Andes), but an overestimation in the east, especially in the NH summer (dry season). LMF22 explained this latter positive bias by a tendency of the IFS to produce too widespread daytime shallow convection after noon. A negative bias around -10% affects the central United States and western Canada during the winter period (Fig.2e). Explaining this particular bias would require using other observations than satellite data, which is beyond the scope of this study. Elsewhere, and away from the terminator, biases over land regions remain within a few percent in reflectance units. In particular, it is worth noting that mean biases are very small over deserts where clear-sky conditions prevail, which gives confidence in the reflectances obtained from the land surface BRDF atlas used in our RTTOV calculations (see further examination in section 4.5).

3.2.2 Correlations

In contrast to biases, which can be affected by both radiative transfer deficiencies and IFS modelling errors, correlations are likely to mainly reflect how accurately the shape, size and location of clouds are predicted by the IFS, compared to satellite observations. Figure 3 shows maps of the reflectance correlations for the two selected periods, over the field of view of each one of the four satellites. For both periods, correlations are above 0.6 over most extratropical regions, but usually below 0.2 in the

tropics, especially over the Pacific Ocean, the Amazon basin and Africa. This worse agreement between IRM and observations in the tropics is to be expected, as a result of the usual challenges in forecasting deep convection over land and sea, as well as trade-wind clouds over tropical oceans. During the local winter, correlations are particularly high (above 0.8) over the eastern Unites States (Fig.3e) and eastern China (Fig.3c), which is likely due to the predominance of usually well-predicted overcast conditions. Smaller regions with correlations below 0.2 can be found in the wintertime over western Canada and the central United States (Fig.3e,f), as well as in western China and Mongolia (Fig.3c). The high skill of the IFS at predicting the few cloud events which affect the otherwise cloud-free regions of South Brazil, South Africa and parts of the Sahara Desert during the local winter (Fig.1b,d) can explain the very high correlations found over these regions in Fig.3f,b,a, respectively. This was easily verified by scrolling through daily simulated and observed images (not shown). In contrast, the seemingly very poor correlations found over truly cloud-free regions such as other parts of the Sahara in Fig.3a,b) should be disregarded, since these are caused by tiny discrepancies in reflectance between IRM and observations.

It is worth noting that correlations against Himawari-8 (Fig.3c,d) are generally higher than those against the three other satellites. This can be partly explained by the fact that the statistics with respect to Himawari-8 have been computed using 3h-range IFS forecast data, therefore very close to the analysis time of 00Z. Indeed, Fig.4 shows that correlations drop by roughly 0.2 when they are computed from (b) 15h-range forecasts starting at 12Z, rather than from (a) 3h-range forecasts starting at 00Z.

3.2.3 Standard deviation ratios

Figure 5 displays maps of the 0.64-μm reflectance standard deviation ratio $SDR = \sigma^{IRM}_{refl} / \sigma^{obs}_{refl}$ during the two periods and for each satellite. Many regions of the globe exhibit *SDR* values close to unity, which indicates that the day-to-day variability of reflectance in IRM often agrees well with satellite observations.

However, while the day-to-day variability is generally slightly overestimated in IRM over extratropical oceans ($1.0 < SDR < 1.4$), it is clearly underestimated over widespread regions of tropical oceans ($0.3 < SDR < 1.0$). The western and central Pacific (Fig.5e-h) and the western Indian Ocean (Fig.5a), and more locally, the stratocumulus regions near the coasts of Morocco, Angola, Peru and Chile are particularly affected during the NH summer (Fig.5b,f). The large negative biases in reflectance (too few clouds in the IFS) that were identified in the latter stratocumulus regions in Fig.2b,f, can explain their low *SDR* values.

Over land, the very large values of *SDR* found during the NH summer over the African and Australian deserts (Fig.5)b,d, as well as over southern Brazil (Fig.5)f, are artefacts of the predominantly cloud-free conditions that were depicted in Fig.1d, and which lead to very low values of standard deviations (see Fig.8e,f and Fig.9e, further down). The same is true over parts of the northern half of Africa in the NH winter (Fig.5)a. Elsewhere over land, *SDR* is often close to 1, which indicates a good agreement with observations.

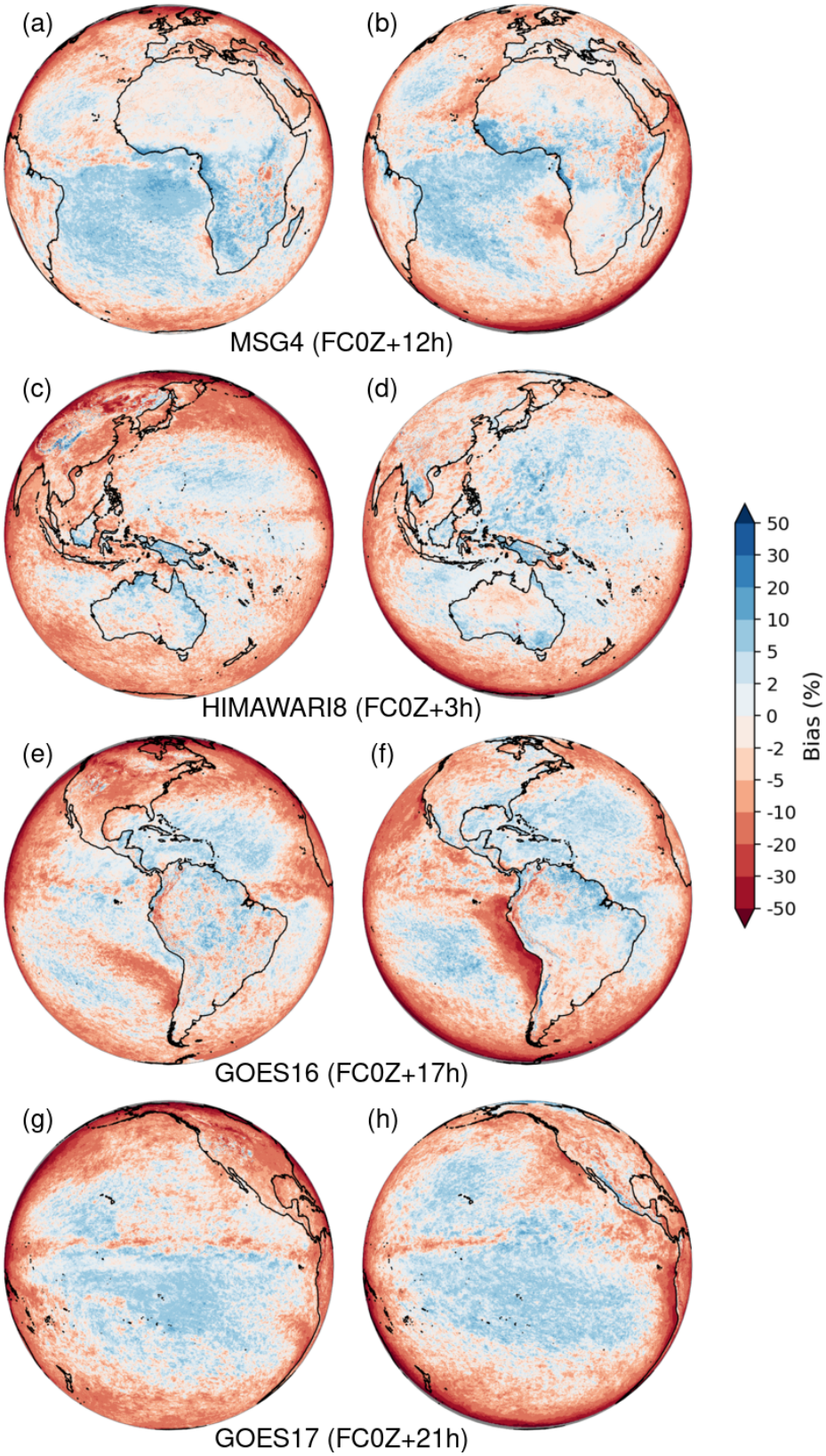

Figure 2: Mean bias in 0.64-µm reflectance between IFS+RTTOV/MFASIS (IRM) and observations over the two selected periods: 15 January-15 February 2021 (left column) and 15 July-15 August 2021 (right column), and for the shortest IFS forecast range corresponding to SSP local noon (see section 2.2 for details). Red (resp. blue) shading indicates that IRM's simulated reflectance is lower (resp. higher) than observed. Rows correspond to the field of view of (a,b) MSG-4, (c,d) Himawari-8, (e,f) GOES-16 and (g,h) GOES-17. Bias is expressed in units of reflectance (percent).

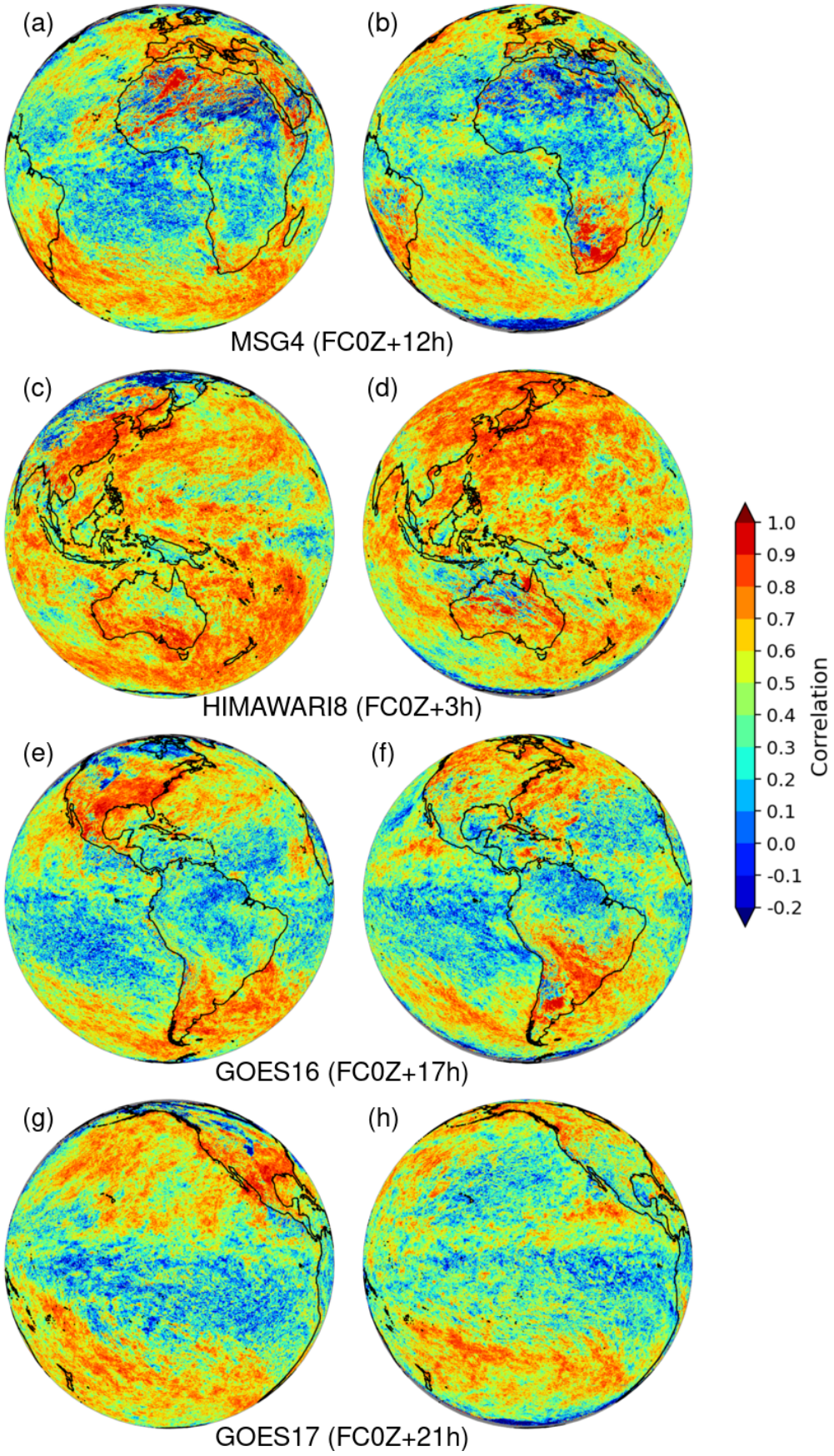

Figure 3: Same as in Fig.2, but for IFS+RTTOV/MFASIS versus observed 0.64-µm reflectance correlation.

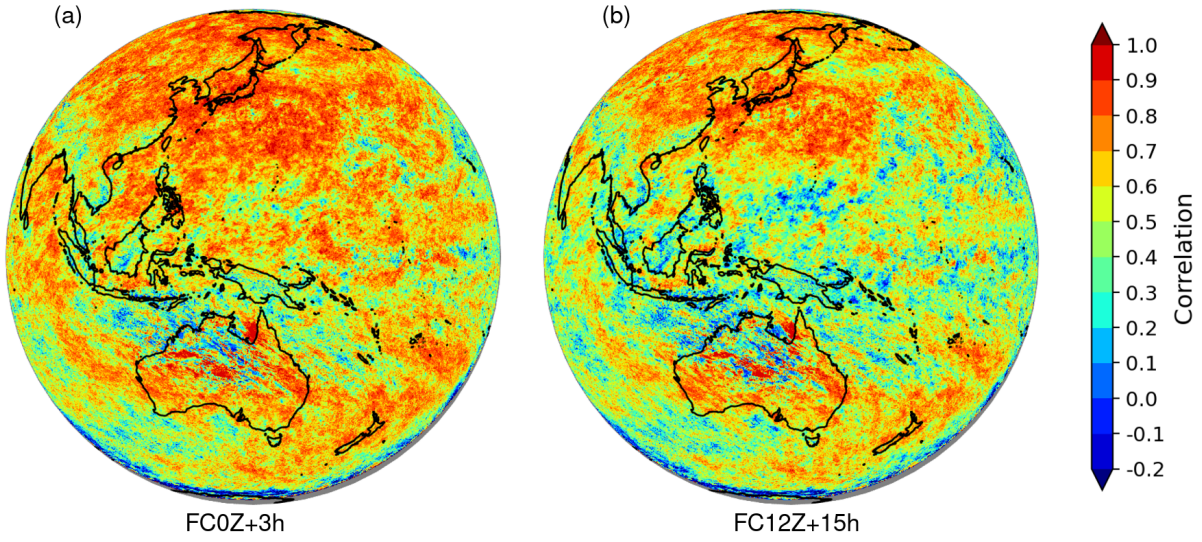

Figure 4: Correlations of IRM and Himawari-8 reflectances over the period 15 July-15 August 2021, computed either (a) from 3h-range forecasts starting at 00Z or (b) from 15h-range forecasts starting at 12Z.

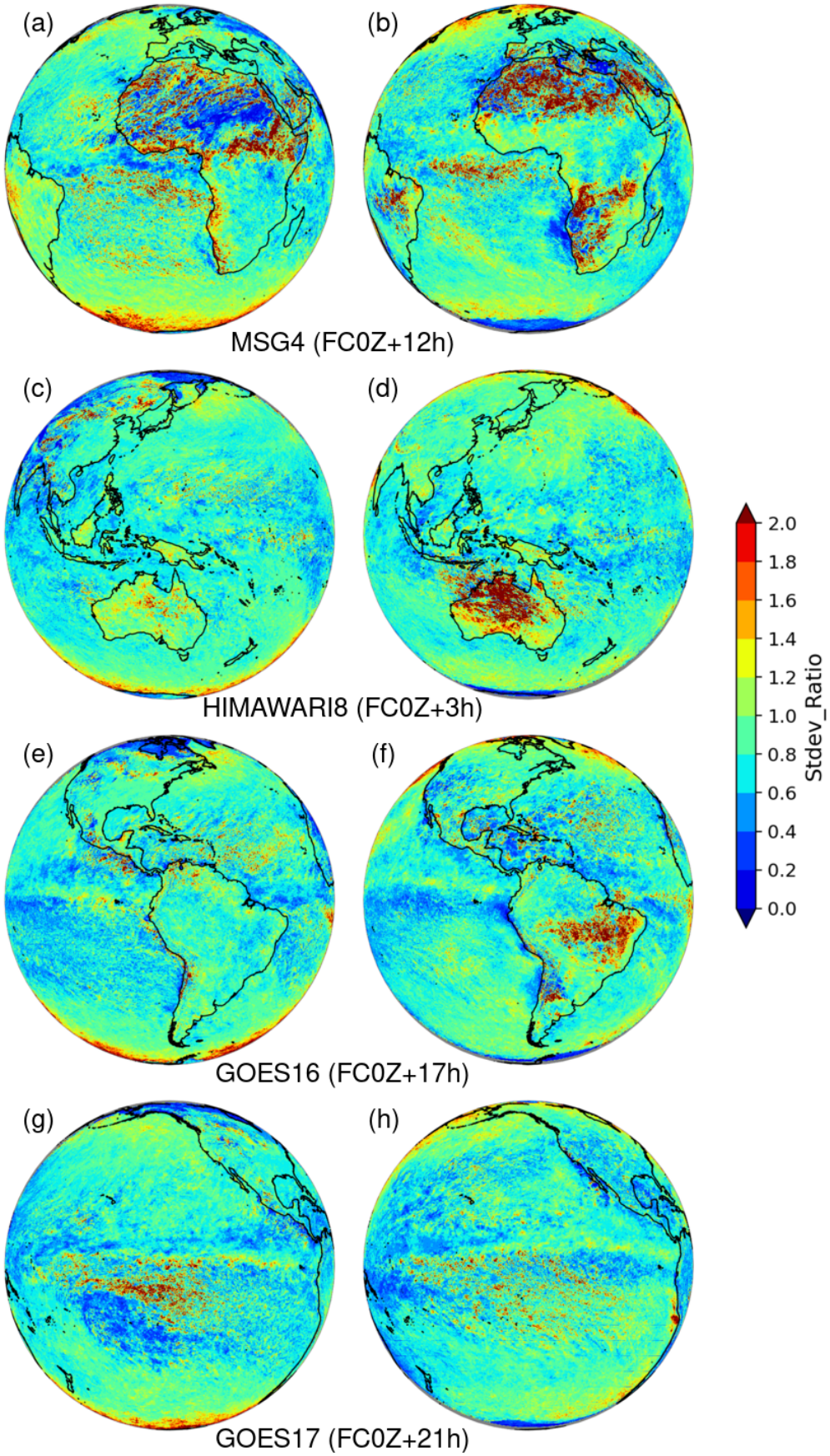

Figure 5: Same as in Fig.2, but for the ratio of the 0.64-µm reflectance standard deviations of IFS+RTTOV/MFASIS and observations (i.e., $\sigma_{refl}^{IRM} / \sigma_{refl}^{obs}$).

3.3 Comparison of IFS versions 47R1 and 47R3

The availability of simulated satellite imagery at visible wavelengths also allows the monitoring of changes made to the IFS model, especially in terms of its ability to represent cloud systems. An illustration is given here, with the comparison of the two most recent operational versions of the IFS, namely 47R1 and 47R3, for the period 15 July-15 August 2021. The most important change in IFS version 47R3 was the in-depth revision of the moist physics package in the forecast model, which affected both the large-scale cloud scheme and the convection scheme (Bechtold *et al.*, 2020).

First, Figures 6 and 7 display mean IRM−observed reflectance biases for IFS version 47R1 (top), 47R3 (middle) and the 47R3−47R1 difference (bottom), for the four satellites and corresponding forecast times (columns; see bottom labels). The usually moderate positive bias found in version 47R1 over most of the tropical oceans has become closer to zero in version 47R3. Furthermore, in Fig.7, the underestimation in 47R1 off the coasts of both California and Peru, which was already explained by a systematic underestimation of maritime stratocumuli in the IFS, is partially reduced in version 47R3. On the other hand, the negative biases located off the Moroccan and Angolan coasts in Fig.6a, which are also due to stratocumuli underestimation in the IFS, are slightly worse with version 47R3 (Fig.6c). Elsewhere, a noticeable bias degradation with 47R3 can be identified (1) in the north of the Amazon basin (stronger reflectance overestimation in Fig.7a,c,e) and (2) over the Ethiopian Highlands (reflectance underestimation in Fig.6a,c,e). In other regions, IRM biases against observations remain comparable in both IFS versions.

Secondly, Figures 8 and 9 compares reflectance standard deviations σ_{refl} calculated from IRM based on IFS versions 47R1 (top panels) and 47R3 (middle panels), as well as from satellite observations (bottom panels). Unsurprisingly, the very low values of σ_{refl} (below 5% in reflectance units) over cloud-free deserts (Sahara, Namibia, Australia) in IRM are unchanged between model versions, and in very good agreement with observations. In contrast, Fig.8a,c,e exhibits a clear increase in σ_{refl} in IRM between versions 47R1 and 47R3 over African regions affected by monsoon precipitation, from Guinea to Sudan. While such increase brings the model closer to observations over Chad and Sudan (as well as over the North Atlantic ITCZ), the day-to-day variability of IRM reflectances from Guinea to Nigeria is overshooting observations in version 47R3. A similar significant increase in IRM σ_{refl} appears north of the equator in South America (Fig.9a,c,e), again overshooting observed values in 47R3. This is consistent with the bias increase that was identified over this region in Fig.7e. Over the Ethiopian Highlands, the two IFS versions lead to comparable underestimations of σ_{refl}, which are consistent with the negative biases evidenced in Fig.6a,c. In the tropical Pacific, Figures 8 and 9 suggest that the clear weakness of day-to-day variability which affected IRM reflectances inside the ITCZ over oceans in 47R1, is reduced in 47R3. However, south of the Pacific and Atlantic ITCZ, the day-to-day variability of simulated reflectances is also reduced in 47R3 compared to 47R1, therefore further away from the observations. In the extratropics, Figures 8 and 9 indicate that IRM σ_{refl} values are larger in 47R3 than in 47R1, therefore in better agreement with satellite data.

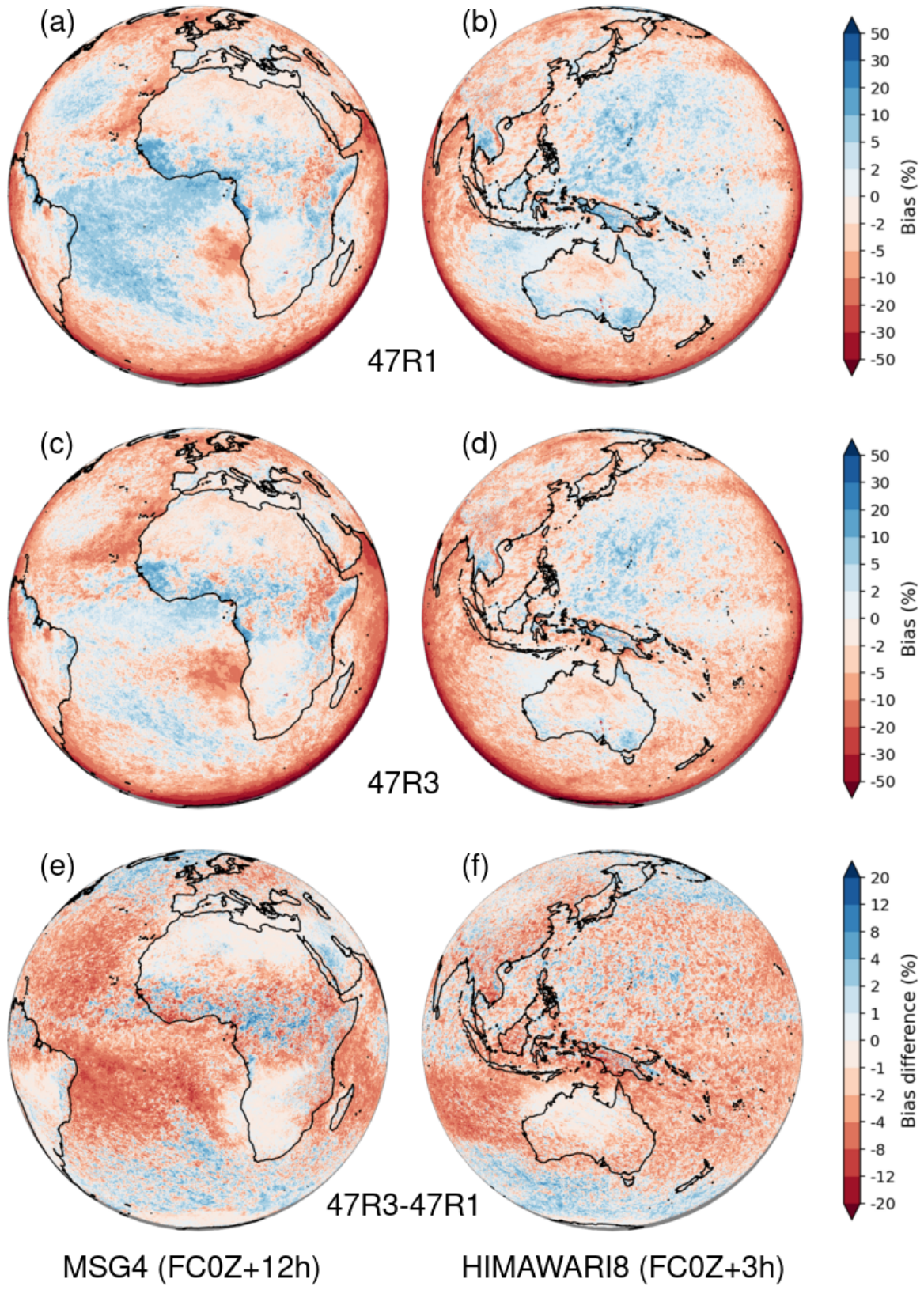

Figure 6: Mean IFS+RTTOV/MFASIS−observation 0.64-µm reflectance bias over the period 15 July-15 August 2021 and over the field of view of MSG-4 (left column) and Himawari-8 (right column). Top row: using IFS version 47R1; Middle row: using IFS version 47R3; Bottom row: 47R3 minus 47R1 bias difference. IRM data are based on the shortest IFS forecast range corresponding to SSP local noon, as indicated at the bottom of each column. All bias statistics are expressed in units of reflectance (percent).

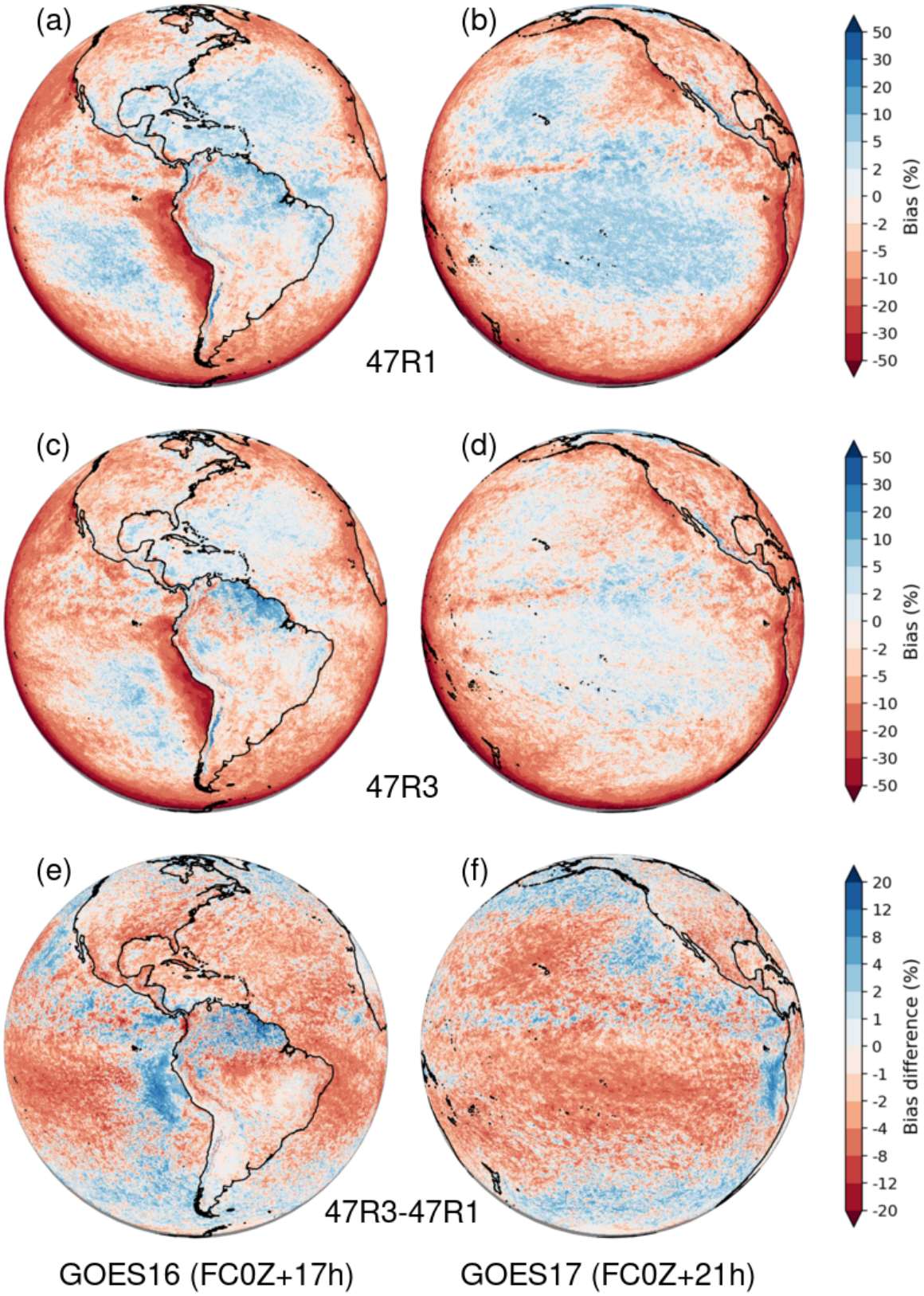

Figure 7: Same as in Fig.6, but over the field of view of GOES-16 (left column) and GOES-17 (right column).

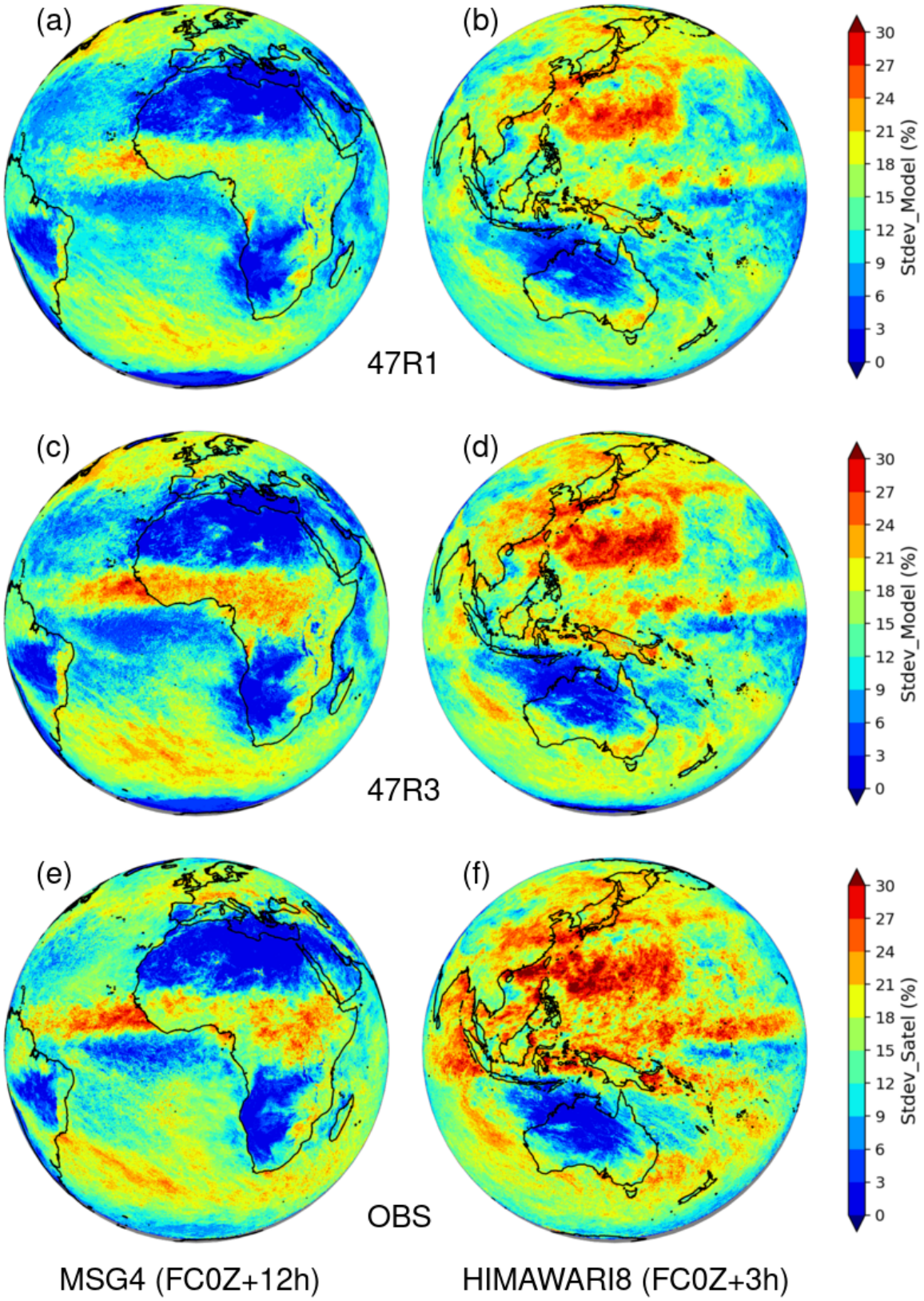

Figure 8: IFS+RTTOV/MFASIS and observation 0.64-µm reflectance standard deviations over the period 15 July-15 August 2021 and over the field of view of MSG-4 (left column) and Himawari-8 (right column). Top row: using IFS version 47R1; Middle row: using IFS version 47R3; Bottom row: from satellite observations. IRM data are based on the shortest IFS forecast range corresponding to SSP local noon, as indicated in the label at the bottom of each column. All standard deviations are expressed in units of reflectance (percent).

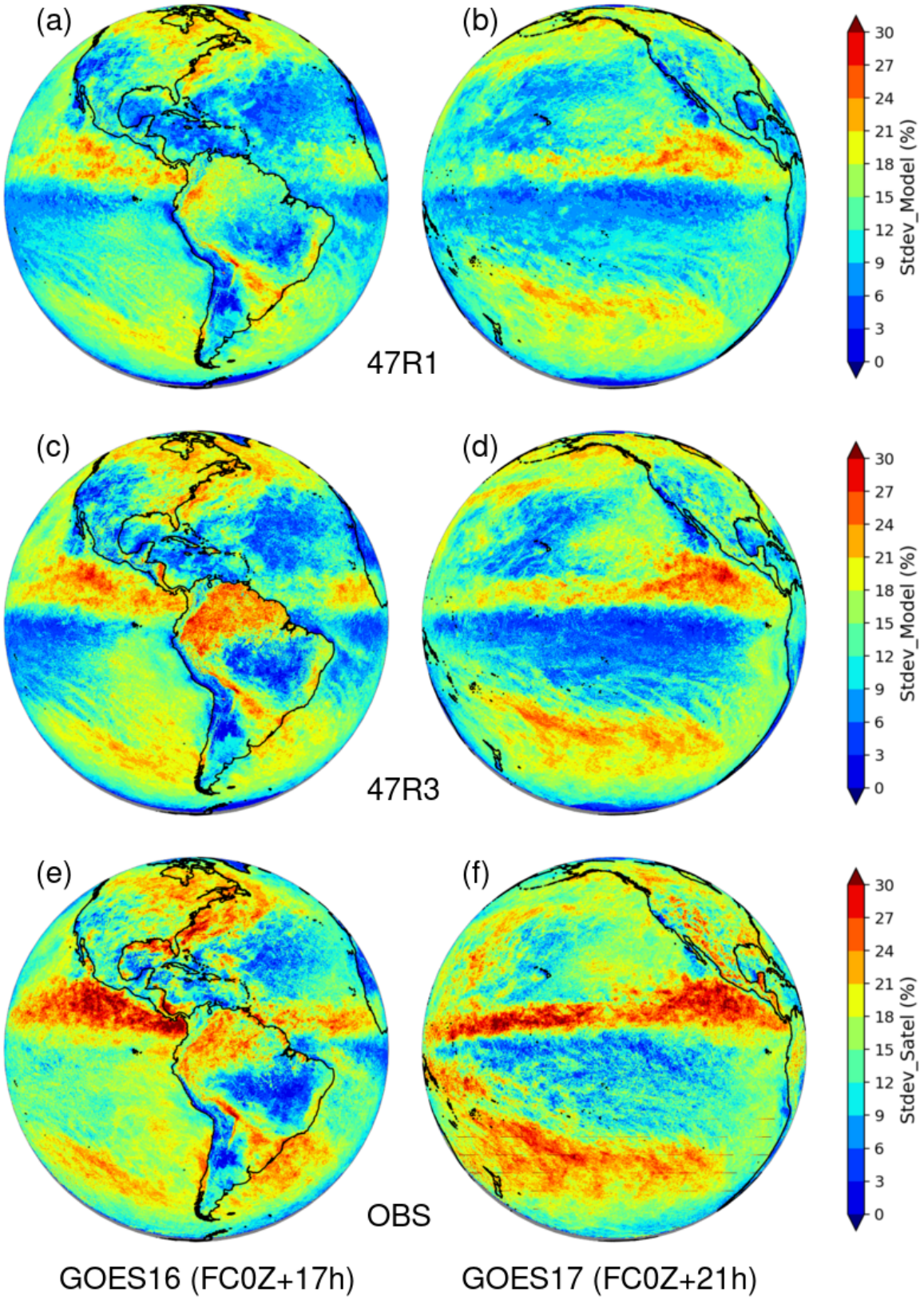

Figure 9: Same as in Fig.8, but over the field of view of GOES-16 (left column) and GOES-17 (right column).

4 Detailed analysis

In this section, some of the most striking discrepancies between IRM simulated and observed reflectances, as identified from monthly statistics in sections 3.2 and 3.3, are further investigated by looking at images for individual days that were found to be well representative of a given issue. The level of representativeness of a selected day was assessed by browsing through the whole month of simulated and observed images. The focus here is on tropical regions, where the largest biases or day-to-day variability differences between IRM and observations are found. One should note that the major discrepancies over the Americas (GOES-16's field of view), which were already presented in LMF22, will not be discussed here.

4.1 Ethiopia and Somalia

First, Fig.10 illustrates a situation (1200 UTC 21 January 2021) which is typical of the positive bias that was identified in Fig.2a over the Ethiopian Highlands during the dry season (NH winter). Figure 11 displays (a) a map of the local orography and 10m wind vector forecast, as well as (b) a vertical cross-section of total condensate amounts along the direction shown in panel (a). On the selected day, Fig.10b suggests that IRM clearly predicts too much shallow convection from the northern part of the highlands down to Lake Victoria, compared to MSG-4 SEVIRI in Fig.10a. Figure 11 indicates that these over-predicted cumulus clouds develop in low wind speed conditions, locally. However, the low-level flow from the Afar Triangle in the north and from the Somali coast in the east is likely to supply moisture to the highlands. Therefore, one can speculate whether an overestimation of this flow in the model might be responsible for the over-prediction of shallow convection in Fig.11b.

As previously illustrated in Fig.2b, this region of Africa is also affected by a tripolar bias during the rainy season (NH summer), with an area of systematic overestimation of reflectances in IRM over the Somali Plains, nested between two regions of clear underestimation over the Ethiopian Highlands and Somali coastline. An illustration of this bias tripole is given in Figure 12 at 1200 UTC 9 August 2021. The low-level circulation and total condensate amounts for that date are also plotted in Fig.13. The deep convection over the Ethiopian mountains is in sharp contrast with the much more stable conditions and low-level clouds associated with the low-level Findlater jet, which prevail over Somalia. It is clear from Fig.12 and Fig.13b that over the Ethiopian Highlands, the IFS does produce deep convective clouds, but with lower reflectances than observed by MSG. Possible reasons for these underestimated reflectances are:

- A genuine underestimation of clouds and precipitation in the IFS.
- A misrepresentation of the diurnal cycle of convection in the IFS.
- An underestimation of reflectances in RTTOV/MFASIS (e.g., due to uncertainties in the assumed cloud optical properties).
- Some missing contribution from 3D convective snow contents which are computed internally in the IFS, but are not archived from ECMWF's operational forecasts (Liam Steele's personal communication). This could only have a noticeable effect in cloud systems where the IFS convective scheme is much more active than the large-scale condensation scheme. Note, however, that including 3D convective snow amounts in RTTOV/MFASIS calculations in the case of 9 August 2021 only led to a very localized, marginal increase in simulated reflectances (not shown).

Figures 12 and 13 also evidence that the remaining monthly bias dipole found over Somalia in Fig.2b is the consequence of both (1) shallow convection extending too far inland in the IFS, and (2) an un-

derestimation of the reflectances of coastal low-level clouds (accompanied by light precipitation). The latter underestimation might be caused by (1) an underprediction of coastal clouds by the IFS or (2) an underestimation of reflectances by RTTOV/MFASIS (e.g., inaccurate optical properties for cloud liquid water).

4.2 From Guinea to the Ivory Coast

Figures 14 and 15 displays a comparison similar to that in section 4.1, but over the region extending from Guinea to the Ivory Coast, at 1200 UTC 15 August 2021. Figure 14 shows that the positive monthly bias in IRM reflectances previously evidenced in Fig.2b, can also be seen in these individual images, with much higher reflectances over land in IRM (panel (b)) between 5 and 15°N. As expected, Fig.15 reminds us that this area affected by substantial precipitation is supplied in moisture by the low-level southwesterly monsoon flow from the tropical Atlantic (panel (a)), with a noticeable enhancement of precipitation near the highest mountain of the region (panel (b), in the centre), on the selected day. One should note that in the model, most of the predicted precipitation over orography in Fig.15b is produced by the large-scale condensation scheme, while convective precipitation only dominates near the coast and over sea (not shown). This suggests that the excessive cloud amounts (and too high reflectances) simulated over the mountains must be associated with large-scale forcing rather than local convective activity. Figure 16 compares IFS precipitation to GPM[6] IMERG[7] estimates (see Huffman *et al.* (2020a,b) for a description of this dataset) over the period 15 July-15 August 2021. It confirms that the IFS (panel (b) produces too much precipitation over the region of interest, especially over the mountains east of 5°W, which is consistent with the reflectance overestimation.

4.3 Sahelian squall lines

Figure 17 gives four examples of African squall lines that are either completely missing or poorly represented in IRM reflectance simulations, compared to MSG-4 SEVIRI observations. Such bad simulated reflectances must significantly contribute to the very low correlations between IRM and MSG-4 reflectances over the Sahel region in Fig.3b.

On 16 July 2021, Fig.17a shows that a well-developed mesoscale convective system is observed at 1200 UTC around 8°W. No equivalent can be found in the simulated image in Fig.17b. Furthermore, SYNOP observations at Bamako (12.6°N/8.0°W) confirmed the occurrence of thundery precipitation between 0930 and 1300 UTC, while the corresponding IFS forecast remained dry (not shown). However, the model did predict significant amounts of convective precipitation in the same area before 0900 UTC, therefore too early (not shown).

On 19 July 2021, a mature convective system is observed at 1200 UTC around 3.5°W in Fig.17c, while simulated reflectances in Fig.17d suggest that weather conditions in the forecast are virtually cloud-free. In fact, a convective system did develop in the model over the same region on that day, but only six hours later (not shown).

On 21 July 2021, the IFS does predict a squall line stretching from 13°N and 17°N, at around 2°W (Fig.17f), but the simulated reflectances of this cloud system look much fainter than observed (Fig.17e). Besides, it was also checked that the model did predict some significant amount of (mostly) convective precipitation throughout that day, over this region (not shown). Therefore, in this third case, a squall line

[6]Global Precipitation Mission
[7]Integrated Multi-satellitE Retrievals for GPM

is forecast by the IFS, but its reflectances are strongly underestimated by IRM. It is worth mentioning that an alternative IRM simulation in which 3D convective snow amounts were included in RTTOV/MFASIS computations (as hypothesized in section 4.1), failed to improve the simulated reflectances in the squall line.

On 4 August 2021, the MSG image at 1200 UTC in (Fig.17g) features a large mesoscale cloud system which stretches between 9°N and 18°N, at a longitude around 7°W. SYNOP observations at Segou (13.4°N/6.2°W) confirmed that this cluster of thunderstorms released a substantial amount of precipitation around that time (not shown). However, Fig.17h shows that the observed cloud system has no equivalent in the IRM simulation at 1200 UTC, with no precipitation in the model (not shown).

It seems worth mentioning that the simulation of reflectances for the four squall lines was not improved when using forecasts run with IFS version 47R3 (therefore not shown). Over the period 15 July-15 August 2021, Fig.16 highlights the clear underestimation of precipitation in the IFS north of 14°N, compared to observations from IMERG, which emphasizes the lack of convective activity in the model over this region. Possible explanations for where there is poor simulation of reflectances in Sahelian squall lines would be the same as those already listed in section 4.1. Besides the well-documented challenges for correctly modelling the generation, life cycle, intensity and size of such convective events (Becker *et al.*, 2021), the scarcity of observations available over the Sahel might also play a role in the frequent mismatch between IRM and MSG, in particular through the potential misrepresentation of easterly waves in ECMWF analyses.

4.4 Central tropical South Pacific

Figure 18 compares GOES-17 ABI observed reflectances to those simulated by IRM using both IFS versions 47R1 and 47R3 forecast data, at 2100 UTC 21 July 2021, over a region of the central tropical South Pacific, usually affected by low-level clouds during this season. It is very clear that, even though the observed and simulated main cloud patterns in Fig.18a,b do exhibit some degree of similarity, the clouds predicted with IFS version 47R1 are far too widespread, compared to observations. It is worth underlining that cloud top heights simulated by the IFS (namely, between 2 and 4 km across the domain) are comparable with those retrieved from observations (not shown). The systematic occurrence of these overly large cloud clusters throughout the month of July 2021 (not shown) explains the positive mean bias in IRM reflectances found over this region in Fig.7b. Besides, one should stress that a similar deficiency of IFS version 47R1 was already evidenced in LMF22 when comparing IRM to GOES-16 reflectances over a nearby region of the Pacific. In fact, the same issue also affects the tropical Atlantic (not shown). Interestingly, Fig.18c shows that IRM reflectances are reduced when using the latest IFS version 47R3, but simulated cloud clusters remain far too large compared to GOES-17. Over the month of July 2021, this translates into the mean bias reduction already highlighted in Fig.7d,f. Unfortunately, it also leads to the undesirable further drop in reflectance day-to-day variability seen in Fig.9b,d,f.

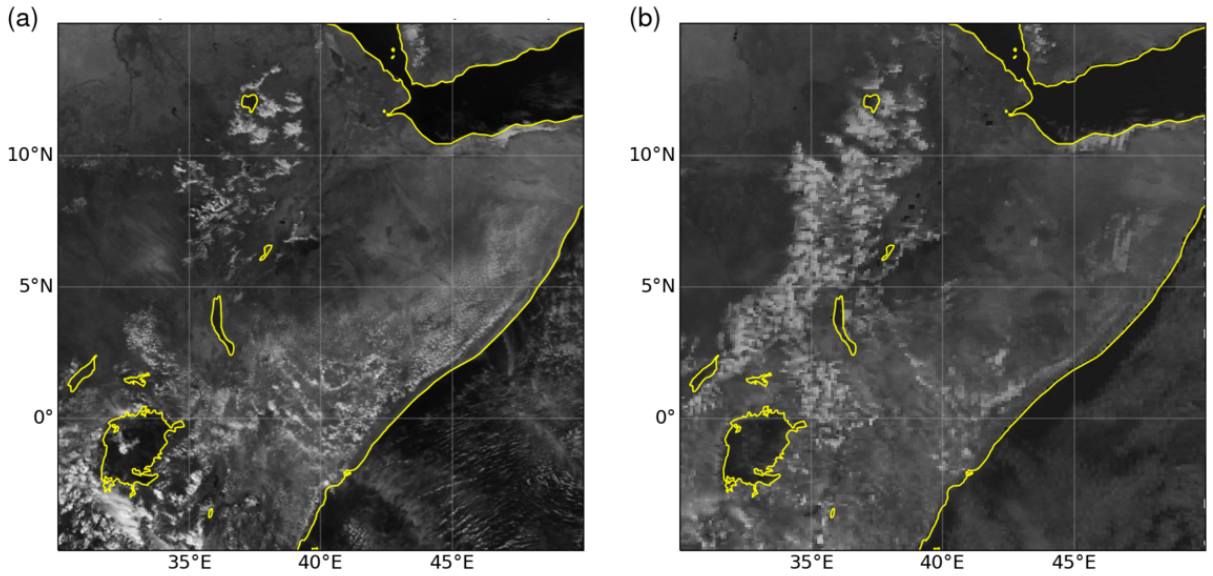

Figure 10: 0.64-µm reflectances from (a) MSG-4 SEVIRI observations and (b) IFS+RTTOV/MFASIS simulation based on IFS version 47R1, over the Ethiopian Highlands and Somalia, and valid at 1200 UTC 21 January 2021. The image simulated with IFS+RTTOV/MFASIS is based on data from a 12h-range forecast starting at 0000 UTC 21 January 2021. Observations and simulation are shown at a resolution of 3 and 9 km, respectively. Note that the same brightness scale is used in the two panels.

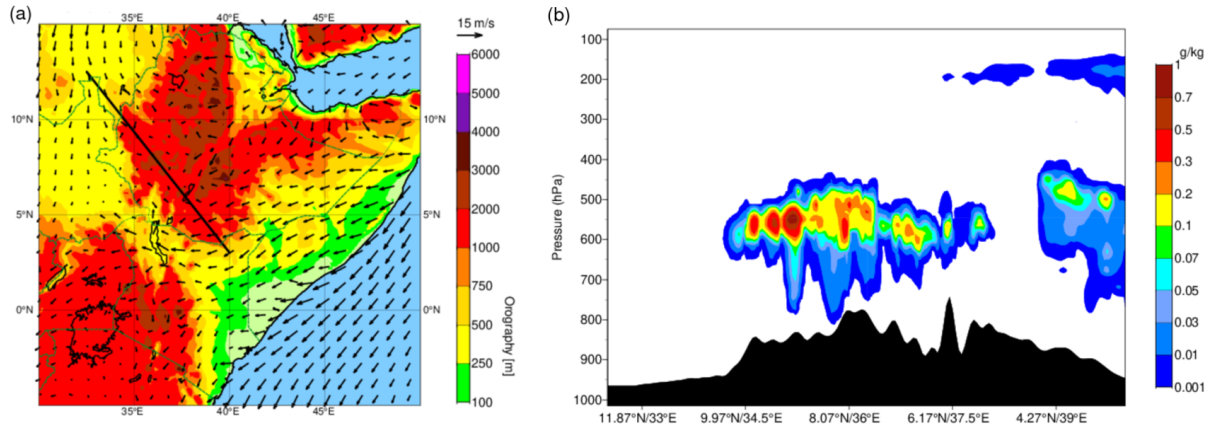

Figure 11: IFS+RTTOV/MFASIS 12h-range forecast over the Horn of Africa: (a) map of 10-metre wind vectors (arrows) and (b) vertical cross-section of total condensate amounts (cloud liquid + cloud ice + rain + snow; in g kg^{-1}), from the 12h-range operational IFS forecast valid at 1200 UTC 21 January 2021. In panel (a), the shading shows the model's orography (in metres), while the solid line indicates the location of the cross-section displayed in panel (b).

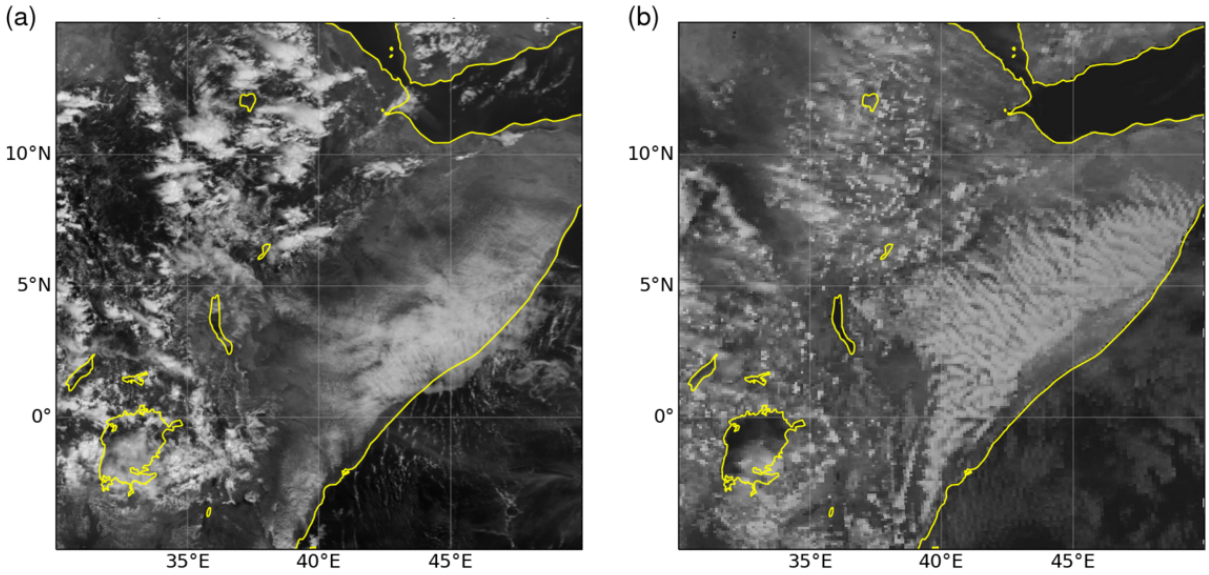

Figure 12: Same as in Fig.10, but valid at 1200 UTC 9 August 2021.

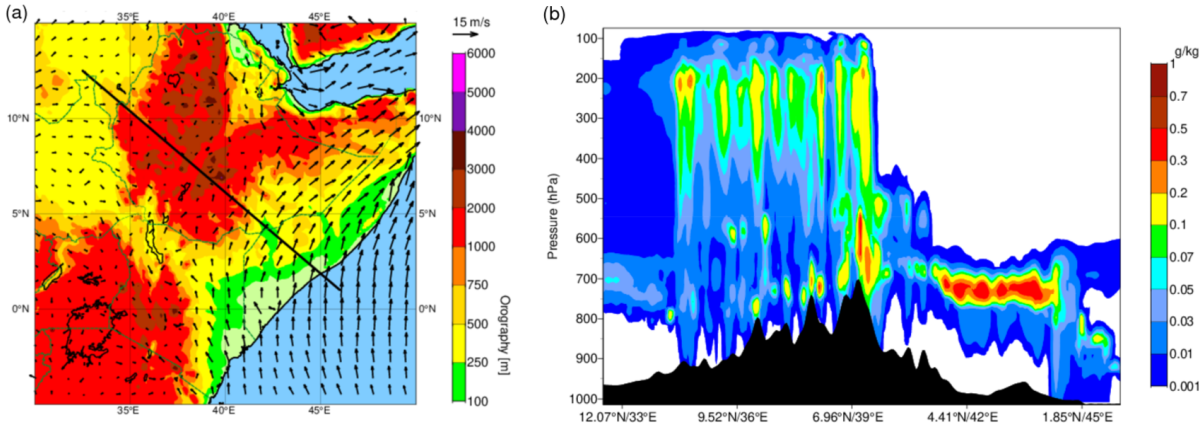

Figure 13: Same as in Fig.11, but valid at 1200 UTC 9 August 2021.

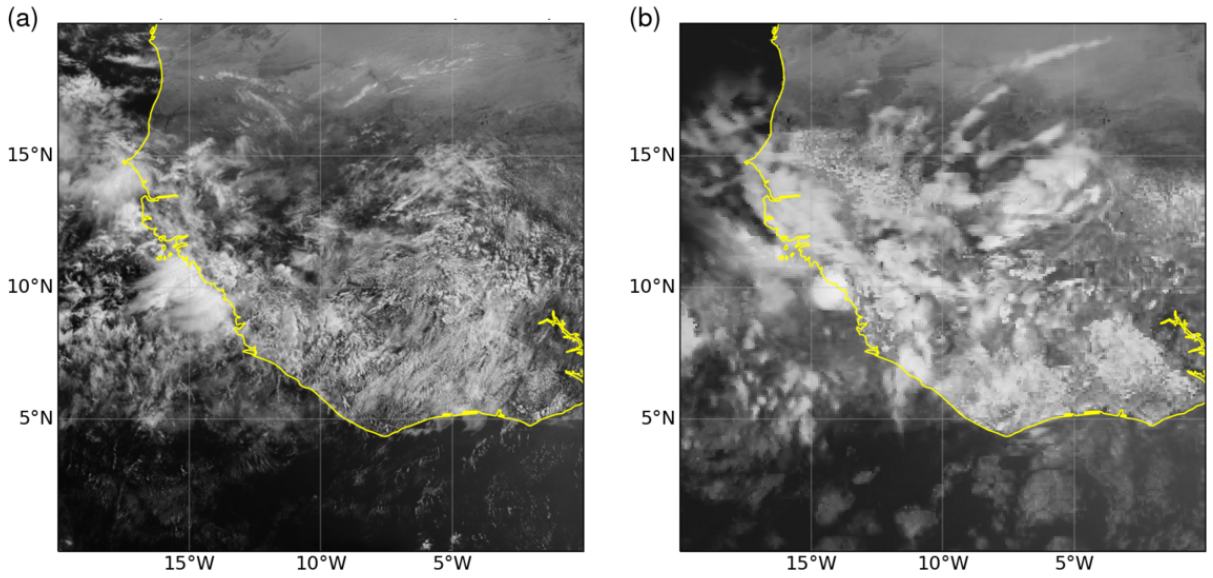

Figure 14: Same as in Fig.12, but over the Guinea Highlands and valid at 1200 UTC 15 August 2021.

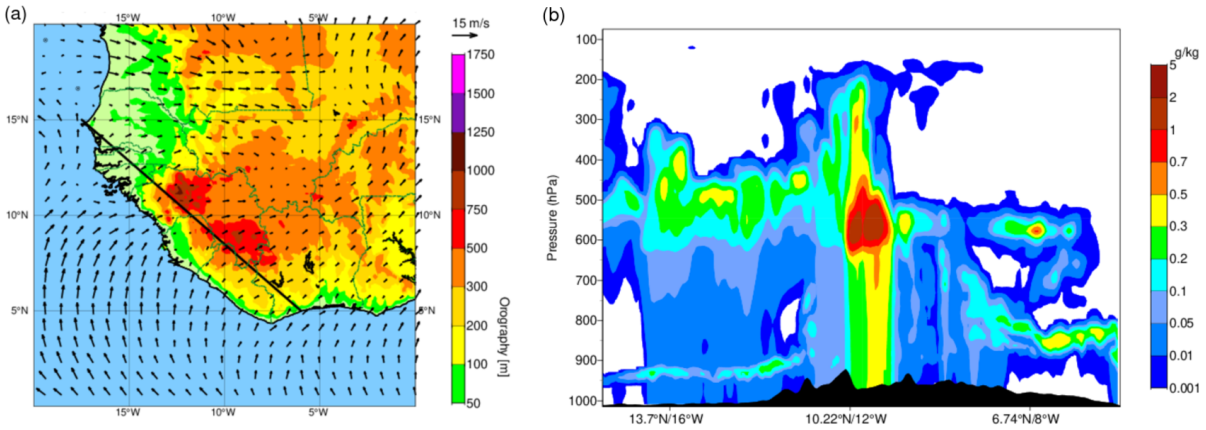

Figure 15: Same as in Fig.13, but over the Guinea Highlands and valid at 1200 UTC 15 August 2021.

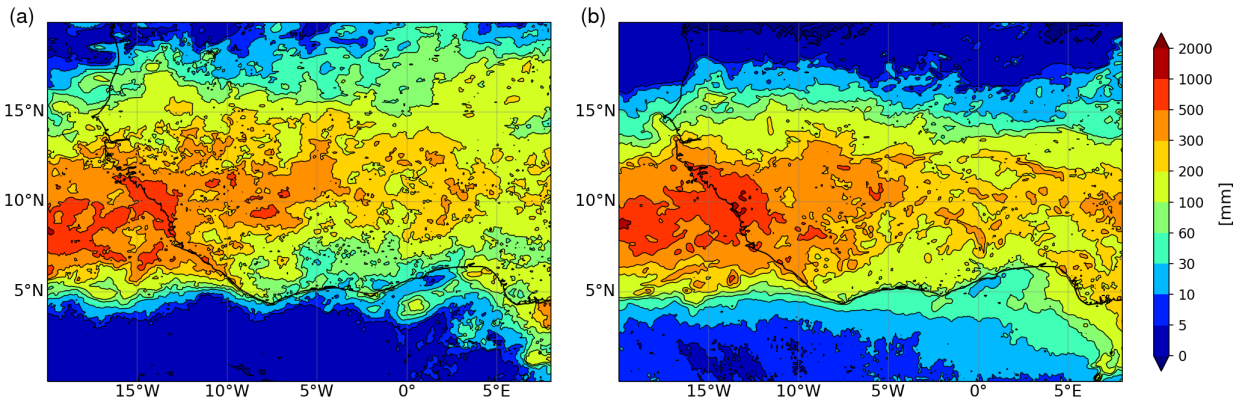

Figure 16: Total precipitation amounts (in mm) from (a) IMERG multi-satellite-and-gauge estimates and (b) IFS forecasts, over West Africa and for the period 15 July-15 August 2021. IFS precipitation is based on daily operational 24h-range forecasts initialized at 0000 UTC (model version 47R1).

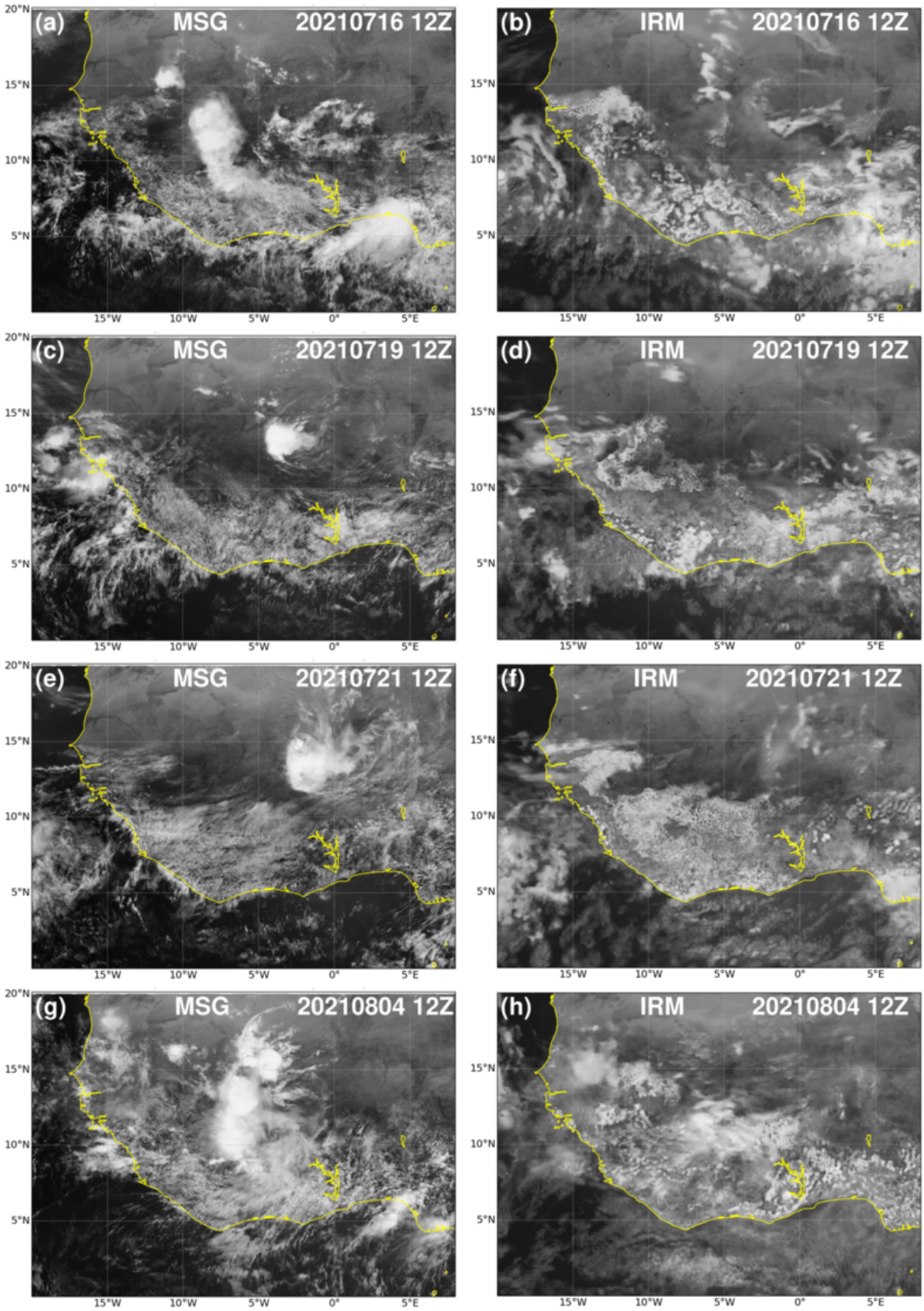

Figure 17: Comparison of 0.64-µm reflectances from (left column) MSG-4 SEVIRI observations and (right column) IFS+RTTOV/MFASIS simulations, for four cases of Sahelian squall lines during summer 2021. Each row corresponds to the valid date indicated at the top of each panel, at 1200 UTC. The simulations used data from 12h-range forecasts starting at 0000 UTC. Observations and simulations are shown at a resolution of 3 and 9 km, respectively.

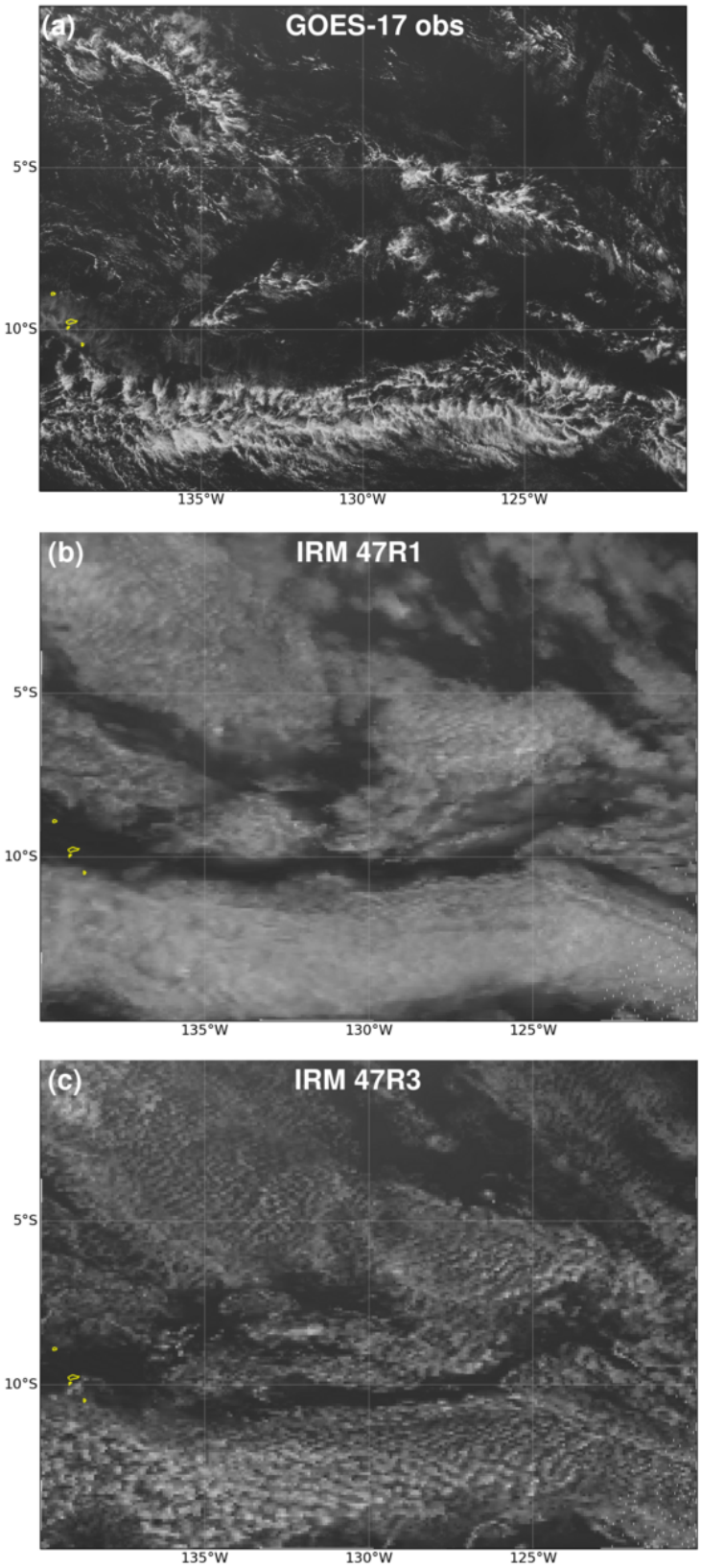

Figure 18: 0.64-µm reflectances from (a) GOES-17 ABI observations, (b) IFS+RTTOV/MFASIS simulation based on IFS version 47R1 and (c) IFS+RTTOV/MFASIS simulation based on IFS version 47R3, over the central tropical South Pacific, and valid at 2100 UTC 21 July 2021. The simulations in (b) and (c) used data from 21h-range forecasts starting at 0000 UTC 21 July 2021. Observations and simulations are shown at a resolution of 1 and 9 km, respectively.

4.5 Assessment of clear-sky reflectances (land surface BRDF atlas)

To assess the relevance of using the monthly land surface BRDF atlas in RTTOV/MFASIS, IRM and GOES-16 0.64-μm reflectances have been compared in clear-sky conditions (no clouds and no significant aerosol) over land. Note that Himawari-8 was not considered here, due to the lack of readily available cloud and aerosol retrievals, nor was GOES-17 because of its predominantly maritime field of view. In the case of IRM, clear-sky reflectances (without clouds and aerosols) come as default outputs from RTTOV/MFASIS, while the GOES-16 cloud mask and aerosol optical depth (AOD) level-2 products (Heidinger and Straka, 2012; NOAA/NESDIS/STAR, 2018) have been employed for selecting cloud-free situations with low aerosol amounts (AOD$<$0.07) in the observations. Furthermore, locations with solar elevations below 40° have been discarded from the statistics to avoid potential uncertainties both in GOES-16 AOD retrievals and in RTTOV/MFASIS simulations. This procedure which is intended to make the comparison of IRM to observations as fair as possible, does imply that the sample size for clear-sky statistics over land is limited to a few thousand points over a whole month. Most of these are located south of the Amazon basin, with a smaller group of points over the United States in the winter.

Figure 19 displays scatter diagrams of IRM versus GOES-16 ABI clear-sky 0.64-μm reflectances over land for both selected periods, valid at 1700 UTC (i.e., SSP noon). Despite the limitation of using fixed BRDF values for a given month in RTTOV/MFASIS, and except for some rare outliers, simulated and observed clear-sky reflectances agree rather well, with a hint of a slight underestimation in IRM for increasing reflectances. Expressed in units of reflectance (%), the root-mean-square difference (RMSD) between IRM and GOES-16 is 1.7 (resp. 1.1) for the winter (resp. summer) month, while the mean bias is -1.2 (resp. -0.3). Prescribing surface BRDF values that vary on a day-to-day basis might help to reduce these small departures in clear-sky reflectance even further.

An attempt to perform a similar evaluation of IRM clear-sky 0.64-μm reflectances over land against MSG-4 SEVIRI observations is also presented in Fig.20, for the period 15 July-15 August 2021. However, one should note that a higher uncertainty may affect this validation due to the unavailability of aerosol information from MSG-4. This means that only the screening of cloudy situations could be applied, resulting in a sample size of 55641 land points, all located either north of 15°N (i.e., over the Sahara) or south of 10°S (not shown). With the latter limitation in mind, Fig.20 evidences the reasonable agreement between IRM and MSG-4 overall, with a mean bias of -1.1% and an RMSD of 2.5% (in reflectance units). The linear fit (blue line) in Fig.20 indicates that IRM slightly underestimates clear-sky reflectances above 30%, which are typical of desert regions. This suggests that surface BRDF values specified in RTTOV's atlas might be slightly too low over the Sahara and the Namib.

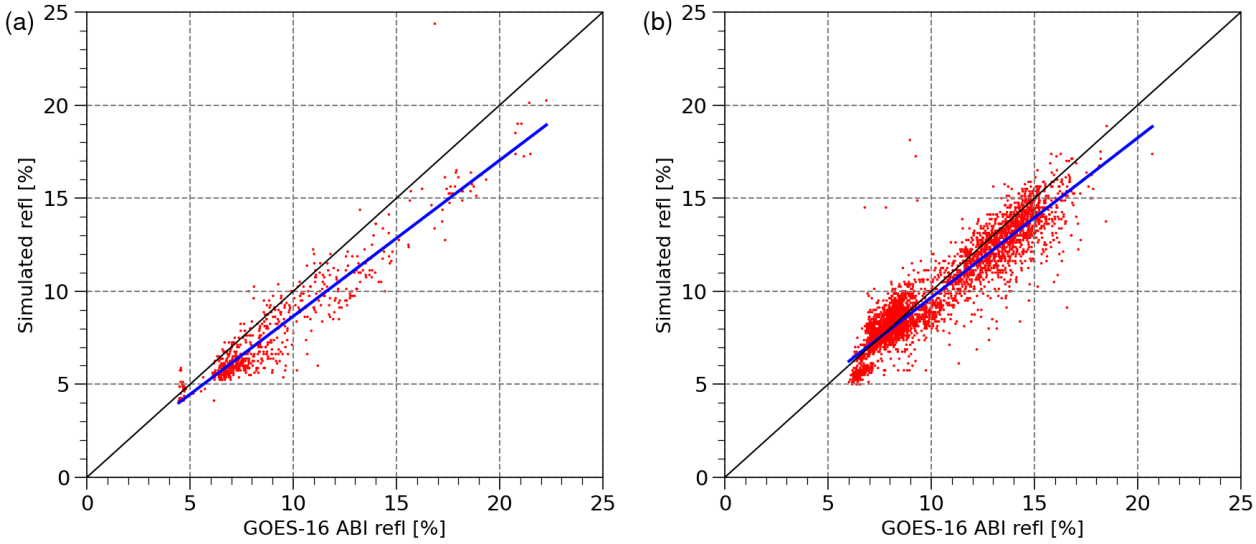

Figure 19: Scatter plot of clear-sky 0.64-µm reflectances over land from GOES-16 ABI observations and IFS+RTTOV/MFASIS simulations based on IFS version 47R1, and valid at 1700 UTC, for periods (a) 15 January-15 February 2021 and (b) 15 July-15 August 2021. Sample size for each period is equal to 618 and 4034, respectively, and the blue line shows the linear fit to each scatter plot. Simulated IFS+RTTOV/MFASIS reflectances are based on data from daily operational 17h-range forecasts starting at 0000 UTC (IFS version 47R1). Observations and simulations have been taken at the same resolution of 9 km (at SSP).

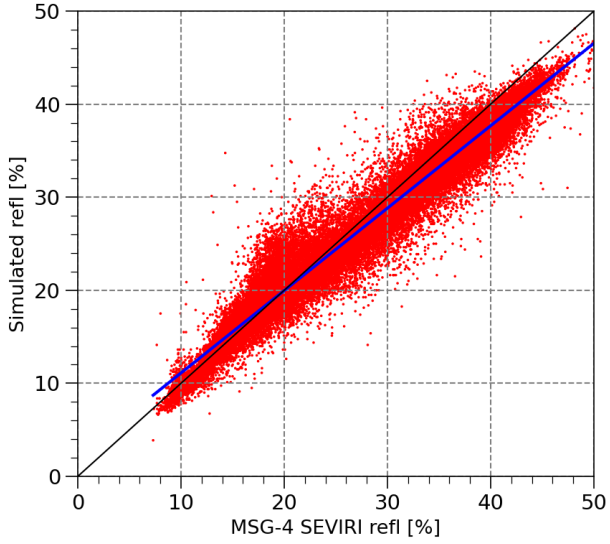

Figure 20: Same as in Fig.19, but against MSG-4 SEVIRI observations at 1200 UTC, over the period 15 July-15 August 2021. Sample size is equal to 55641. Simulated IFS+RTTOV/MFASIS reflectances are based on data from daily operational 12h-range forecasts starting at 0000 UTC (IFS version 47R1).

5 Summary and conclusions

As a follow-up to Lopez *et al.* (2022), 0.64-μm reflectances simulated by running RTTOV/MFASIS on IFS operational short-range forecast data (at 9-km resolution; IFS version 47R1) have been validated against MSG-4, Himawari-8, GOES-16 and GOES-17 reflectances, over two 1-month-long periods.

This study has confirmed that the main deficiency of RTTOV/MFASIS radiative transfer is the systematic negative bias in simulated reflectances near the terminator, which results from interpolation errors when interpolating MFASIS's look-up table at solar elevations below 10°. Away from the terminator, the best agreement between simulated and observed reflectances is found in the extratropics, with generally low mean biases and high correlations with respect to observations. In the tropics, several issues, most of them attributable to the IFS itself, have been identified or confirmed:

- Too large cloud clusters forecast in trade-wind regions in the tropical Pacific and Atlantic oceans;
- Underprediction of stratocumuli off the coasts of California, Chile, Peru, Morocco and Angola, with erroneous closed-cell convection compared to observed open-cell convection (see LMF22 for details);
- Overestimation of shallow convective clouds over the Ethiopian Highlands in NH winter;
- Underestimation of deep convective clouds over the Ethiopian Highlands in NH summer;
- Overestimation of clouds (and precipitation) inland, along the western coast of Africa, north (resp. south) of the equator in the NH summer (resp. winter);
- Occasional misrepresentation of squall lines over West Africa during the rainy season, (either total absence or mistiming by several hours, or systematic under-estimation of reflectances). Possible reasons for this problem (in decreasing order of likelihood) are (1) the lower quality of the forecasts' initial conditions due to the lack of local observations in 4D-Var analyses; (2) some difficulties in the IFS to simulate the life cycle of some mesoscale convective events; (3) the specification of inadequate convective cloud properties in RTTOV/MFASIS; and (4) some small missing contribution from convective hydrometeors in reflectance computations.

In addition, validation results for simulated reflectances using IFS versions 47R3 and 47R1 have also been intercompared over the summer month. A clear reduction of mean biases in most regions over tropical oceans, as well as an improved day-to-day variability inside the ITCZ and in most monsoon precipitating regions, constitute the major benefits brought by version 47R3. However, version 47R3 does also show the following main degradations, compared to 47R1:

- Day-to-day variability of simulated reflectances has become too high in the West Sahelian and Amazonian monsoon regions (with a corresponding increase in mean bias);
- South of the central Pacific and Atlantic ITCZ, the underprediction of day-to-day variability of simulated reflectances has worsened. This is because reflectances in 47R3 over these maritime regions are lower than in 47R1, while simulated low-level cloud clusters remain oversized.

Finally, the good agreement between simulated and GOES-16 ABI clear-sky reflectances over land has confirmed that surface BRDF values from the monthly atlas used in RTTOV/MFASIS computations can be considered as reasonably accurate, at least over the sampled cloud- and aerosol-free locations of the American continent. Similarly, IRM and MSG-4 SEVIRI cloud-free reflectances over land seem to be fairly close (including over African deserts), despite the impossibility to screen out aerosols from MSG data.

In the future, assessing the impact of including aerosols on simulated reflectances would be interesting, but this would require either substantial modifying RTTOV/MFASIS or using another offline simula-

tor, such as FLOTSAM developed by Robin Hogan (ECMWF). Repeating this validation exercise with version 13 of RTTOV/MFASIS would be very interesting and would also allow us to obtain statistics over the Indian Ocean and Western Asia using data from EUMETSAT's MSG-2 satellite. The findings from this study might also be useful for the planned assimilation of visible reflectances in ECMWF's 4D-Var system (quality control; observation screening), should MFASIS be selected as the visible reflectance observation operator. Finally, the validation of simulated solar reflectances will also be part of the evaluation of kilometre-scale experiments that will be run in the course of the DestinE and nextGEMS projects.

Acknowledgements

We are very grateful to:

- EUMETSAT for making MSG-4 SEVIRI observations available via their Data Store;
- the National Oceanic and Atmospheric Administration (NOAA, USA) for granting access to the GOES ABI data, via their Comprehensive Large Array-data Stewardship System (CLASS).
- the National Aeronautics and Space Administration (NASA, USA) for providing the GPM IMERG precipitation data.
- Jérôme Vidot of the "Centre d'Etudes en Météorologie Satellitaire" (CEMS, France) and the Japan Meteorological Agency (JMA) for providing Himawari AHI data.

Special thanks also go to Chris Burrows (ECMWF) for his help in gaining access to the Himawari data. Our ECMWF colleagues Richard Forbes, Peter Bechtold and Tony McNally should be acknowledged for their comments on the final version of this document, and Leonhard Scheck (Ludwig Maximilian Universiy, Munich) for his valuable advice on MFASIS.

References

Baum, B. A., Yang, P., Heymsfield, A. J., Schmitt, C. G., Xie, Y., Bansemer, A., Hu, Y.-X. and Zhang, Z. (2011). Improvements in Shortwave Bulk Scattering and Absorption Models for the Remote Sensing of Ice Clouds. *J. Appl. Meteor. Climatol.*, **50**(5), 1037–1056, doi:10.1175/2010JAMC2608.1.

Bechtold, P., Forbes, R. M., Sandu, I., Lang, S. and Ahlgrimm, M. (2020). A major moist physics upgrade for the IFS. *ECMWF Newsletter*, (164), Available at https://www.ecmwf.int/en/newsletter/164/meteorology/major-moist-physics-upgrade-ifs.

Becker, T., Bechtold, P. and Sandu, I. (2021). Characteristics of convective precipitation over tropical Africa in storm-resolving global simulations. *Quart. J. Roy. Meteor. Soc.*, **147**(741), 4388–4407, doi:10.1002/qj.4185.

Courtier, P., Thépaut, J.-N. and Hollingsworth, A. (1994). A strategy for operational implementation of 4D-Var using an incremental approach. *Quart. J. Roy. Meteor. Soc.*, **120**, 1367–1388.

Elfouhaily, T., Chapron, B., Katsaros, K., and Vandemark, D. (1997). A unified directional spectrum for long and short wind-driven waves. *J. Geophys. Res.*, **102**(C7), 15781–15796, doi:10.1029/97JC00467.

Heidinger, A. and Straka, W. C. I. (2012). Algorithm Theoretical Basis Document: ABI Cloud Mask. *Technical report*, NOAA/NESDIS, NOAA NESDIS Center for Satellite Applications and

Research, College Park, MD, USA; https://www.star.nesdis.noaa.gov/goesr/documents/ATBDs/-Baseline/ATBD_GOES-R_Cloud_Mask_v3.0_July%202012.pdf, 106 pages.

Hess, M., Koepke, P. and Schult, I. (1998). Optical Properties of Aerosols and Clouds: The Software Package OPAC. *Bull. Amer. Meteor. Soc.*, **79**(5), 831–844, doi:10.1175/1520-0477(1998)079⟨0831:OPOAAC⟩2.0.CO;2.

Huffman, G. J., Bolvin, D. T., Braithwaite, D., Hsu, K., Joyce, R., Kidd, C., Nelkin, E. J., Sorooshian, S., J. Tan, J. and Xie, P. (2020a). Algorithm Theoretical Basis Document (ATBD) Version 06 for the NASA Global Precipitation Measurement (GPM) Integrated Multi-satellitE Retrievals for GPM (IMERG). *Technical report*, NASA, GPM Project, Greenbelt, MD, 38 pp., https://gpm.nasa.gov/sites/default/files/2020-05/IMERG_ATBD_V06.3.pdf.

Huffman, G. J., Bolvin, D. T., Braithwaite, D., Hsu, K., Joyce, R., Kidd, C., Nelkin, E. J., Sorooshian, S., Stocker, E. F., Tan, J., Wolff, D. and Xie, P. (2020b). *Integrated Multi-satellitE Retrievals for the Global Precipitation Measurement (GPM) mission (IMERG)*, *Adv. Global Change Res.*, Vol. 67, chapter 19, pp. 343–353. Springer Nature, Dordrecht, Netherlands, doi:10.1007/978-3-030-24568-9_19, ISBN 978-3-030-24567-2 / 978-3-030-24568-9 (eBook).

JMA (2017). Himawari-8/9 Himawari Standard Data User's Guide. *Technical report*, JMA, Japan Meteorological Agency, Tokyo, Japan; https://www.data.jma.go.jp/mscweb/en/himawari89/space_segment/-hsd_sample/HS_D_users_guide_en_v13.pdf, 16 pages.

Lopez, P., Matricardi, M. and Fielding, M. (2022). Validation of IFS+RTTOV/MFASIS solar reflectances against GOES-16 ABI observations. *Technical report*, ECMWF, Reading, UK, doi:10.21957/mprjictvg, Technical Memorandum 892, available at https://www.ecmwf.int/node/20332, 27 pages.

McFarquhar, G. M., Iacobellis, S. and Sommerville, R. C. J. (2003). SCM Simulations of Tropical Ice Clouds Using Observationally Based Parameterizations of Microphysics. *J. Climate*, **16**(11), 1643–1664, doi:10.1175/1520-0442(2003)016⟨1643:SSOTIC⟩2.0.CO;2.

NOAA/NESDIS/STAR (2018). GOES-R Advanced Baseline Imager (ABI) Algorithm Theoretical Basis Document For Suspended Matter/Aerosol Optical Depth and Aerosol Size Parameter. *Technical report*, NOAA/NESDIS, NOAA NESDIS Center for Satellite Applications and Research, College Park, MD, USA; https://www.star.nesdis.noaa.gov/goesr/documents/ATBDs/Baseline/ATBD_GOES-R_Aerosol_Optical_Depth_v4.2_Feb2018.pdf, 112 pages.

Saunders, R., Hocking, J., Turner, E., Rayer, P., Rundle, D., Brunel, P., Vidot, J., Roquet, P., Matricardi, M., Geer, A., Bormann, N. and Lupu, C. (2018). An update on the RTTOV fast radiative transfer model (currently at version 12). *Geosci. Model Dev.*, **11**, 2717–2737, doi:10.5194/gmd-11-2717-2018.

Scheck, L., Frèrebeau, P., Buras-Schnell, R. and Mayer, B. (2016). A fast radiative transfer method for the simulation of visible satellite imagery. *J. Quant. Spectrosc. Radiat. Transf.*, **175**, 54–67, doi:10.1016/j.jqsrt.2016.02.008.

Schmid, J. (2000). The SEVIRI intrument. *Technical report*, ESA, European Space Agency, Noordwijk, Netherlands; https://www-cdn.eumetsat.int/files/2020-04/pdf_ten_msg_seviri_instrument.pdf, 10 pages.

Schmit, T. J., Griffith, P., Gunshor, M. M., Daniels, J. M., Goodman, S. J. and Lebair, W. J. (2017). A closer look at the ABI on GOES-R. *Bull. Amer. Meteor. Soc.*, **98**(4), 681–698, doi:10.1175/BAMS-D-15-00230.1.

Schmit, T. J., Gunshor, M. M., Menzel, W. P., Gurka, J. J., Li, J. and Bachmeier, A. S. (2005). Introducing the next-generation advanced baseline imager on GOES-R. *Bull. Amer. Meteor. Soc.*, **86**(8), 1079–1096, doi:10.1175/BAMS-86-8-1079.

Steele, L., Benedetti, A., Matricardi, M., Geer, A. and Lean, P. (2022). Initial results of monitoring cloudy visible radiances. *ECMWF Newsletter*, (171), Available at https://www.ecmwf.int/en/newsletter/171/news/initial-results-monitoring-sscloudy-visible-radiances.

Vidot, J. and Borbás, E. (2014). Land surface VIS/NIR BRDF atlas for RTTOV-11: model and validation against SEVIRI land SAF albedo product. *Quart. J. Roy. Meteor. Soc.*, **140**, 2186–2196, doi:10.1002/qj.2288.